



# The MUSCLES Extension for Atmospheric Transmission Spectroscopy: UV and X-Ray Host-star Observations for JWST ERS & GTO Targets

Patrick R. Behr<sup>1,2</sup> , Kevin France<sup>1,2</sup> , Alexander Brown<sup>3</sup> , Girish Duvvuri<sup>1,3</sup> , Jacob L. Bean<sup>4</sup> , Zachory Berta-Thompson<sup>1,3</sup> , Cynthia Froning<sup>5</sup> , Yamila Miguel<sup>6</sup> , J. Sebastian Pineda<sup>2</sup> , David J. Wilson<sup>1,2</sup> , and Allison Youngblood<sup>7</sup>

<sup>1</sup>Department of Astrophysical & Planetary Sciences, University of Colorado Boulder, Boulder, CO 80309, USA

<sup>2</sup>Laboratory for Atmospheric and Space Physics, University of Colorado Boulder, Boulder, CO 80303, USA

<sup>3</sup>Center for Astrophysics and Space Astronomy, University of Colorado Boulder, Boulder, CO 80309, USA

<sup>4</sup>Department of Astronomy & Astrophysics, University of Chicago, Chicago, IL 60637, USA

<sup>5</sup>Department of Astronomy, University of Texas Austin, Austin, TX 78712, USA

<sup>6</sup>Leiden Observatory/SRON, Leiden, The Netherlands

<sup>7</sup>NASA Goddard Spaceflight Center, Greenbelt, MD 20771, USA

Received 2023 April 4; revised 2023 May 30; accepted 2023 June 2; published 2023 June 28

## Abstract

X-ray through infrared spectral energy distributions (SEDs) are essential for understanding a star's effect on exoplanet atmospheric composition and evolution. We present a catalog of panchromatic SEDs, hosted on the Barbara A. Mikulski Archive for Space Telescopes, for 11 exoplanet-hosting stars that have guaranteed JWST observation time as part of the ERS or GTO programs but have no previous UV characterization. The stars in this survey range from spectral type F4-M6 (0.14–1.57  $M_{\odot}$ ), rotation periods of 4–132 days, and ages of approximately 0.5–11.4 Gyr. The SEDs are composite spectra using data from the Chandra X-ray Observatory and XMM-Newton, the Hubble Space Telescope, BT-Settl stellar atmosphere models, and scaled spectra of proxy stars of similar spectral type and activity. From our observations, we have measured a set of UV and X-ray fluxes as indicators of stellar activity level. We compare the chromospheric and coronal activity indicators of our exoplanet-hosting stars to the broader population of field stars and find that a majority of our targets have activity levels lower than the average population of cool stars in the solar neighborhood. This suggests that using SEDs of stars selected from exoplanet surveys to compute generic exoplanet atmosphere models may underestimate the typical host star's UV flux by an order of magnitude or more, and consequently, that the observed population of exoplanetary atmospheres receive lower high-energy flux levels than the typical planet in the solar neighborhood.

*Unified Astronomy Thesaurus concepts:* Dwarf stars (2053); Exoplanet atmospheres (487); Hubble Space Telescope (761); James Webb Space Telescope (2291); Ultraviolet spectroscopy (2284); Planet hosting stars (1242)

## 1. Introduction

The NASA Exoplanet Archive lists over 5000 confirmed exoplanets across nearly 4000 distinct systems. Estimates from Kepler observations predict exoplanet occurrence rates around F-, G-, and K-type stars of ~10%–60% (Traub 2012; Fressin et al. 2013; Kopparapu 2013; Kunimoto & Bryson 2020) and up to 80% or more for M dwarf stars (Dressing & Charbonneau 2015; Bryson et al. 2020). As the number of confirmed exoplanets increases, so too does the opportunity to characterize the composition and evolution of exoplanetary atmospheres. Atmospheric transmission spectroscopy with the James Webb Space Telescope (JWST) is currently making the highest-quality observations to date of exoplanetary atmospheres. These observations are providing our first molecular inventories of gaseous exoplanets (JWST Transiting Exoplanet Community Early Release Science Team et al. 2023) and are proving the first direct evidence for UV-driven photochemistry on planets beyond the solar system (Tsai et al. 2022). As is now being shown by JWST, the UV spectrum of a planet's host star drives photochemistry and photoionization in exoplanetary

atmospheres, which in turn influences the overall composition of the atmosphere (Moses et al. 2011; Venot et al. 2013; Miguel & Kaltenegger 2014; Miguel et al. 2015), the formation of photochemical hazes and aerosols (He et al. 2018; Kawashima & Ikoma 2018; Kawashima et al. 2019), and powers atmospheric escape in both gaseous and terrestrial planets (Vidal-Madjar et al. 2004; Murray-Clay et al. 2009; Johnstone et al. 2015). Thus, knowledge of the host star's UV spectrum is critical to the interpretation of current and future exoplanetary atmosphere observations.

### 1.1. Stellar UV Effects on Atmospheric Chemistry and Escape of Neptune- to Jupiter-sized Planets

Spectral observations of molecules containing oxygen, nitrogen, and carbon are considered to be good candidates for potential biosignatures. Molecular reservoirs for these elements vary with pressure and temperature; in the upper atmospheres of hot planets with  $700\text{ K} \lesssim T \lesssim 1500\text{ K}$ , oxygen, nitrogen, and carbon are typically contained in  $\text{H}_2\text{O}$ ,  $\text{N}_2$ , and CO (Burrows & Orton 2010; Madhusudhan et al. 2016; Gao et al. 2021). These molecules all have large wavelength-dependent photodissociation cross sections in the UV, typically peaking at less than  $1300\text{ \AA}$  (Lloyd et al. 2016). Thus, in the upper atmosphere of these planets, photochemical effects from UV irradiation can dominate the atmospheric composition,

destroying  $\text{NH}_3$ ,  $\text{N}_2$ ,  $\text{CO}$ ,  $\text{CH}_4$ , and  $\text{H}_2\text{O}$ , and leading to buildups of  $\text{H}$ ,  $\text{HCN}$ ,  $\text{C}_2\text{H}_2$ ,  $\text{N}$ , and  $\text{C}$  (Zahnle et al. 2009; Line et al. 2010; Moses et al. 2011; Miguel & Kaltenegger 2014). There is also evidence that increased UV radiation plays a role in creating the observed temperature inversion in hot-Jupiter atmospheres, where temperature increases with altitude (Zahnle et al. 2009; Knutson et al. 2010; Lothringer & Barman 2019; Fu et al. 2022).

The >5000 confirmed exoplanets so far exhibit a wide range of masses, from sub-Earth to tens of Jupiter masses, as well as orbital periods ranging from hours to tens of years. However, there is a notable dearth of Neptune-mass planets ( $0.03 \lesssim M/M_J \lesssim 0.3$ ) with short orbital periods of  $\lesssim 5$  days, known as the “Neptune desert” (Szabó & Kiss 2011; Mazeh et al. 2016). Owen & Lai (2018) proposed that a combination of high-eccentricity migration and photoevaporation can explain the presence of this desert. In order to quantify photoevaporation processes, we must understand the UV irradiation experienced by the exoplanet. Extreme-UV (EUV;  $\sim 100\text{--}912 \text{ \AA}$ ) radiation, elevated by the small semimajor axes of these planets, is capable of heating the atmosphere to temperatures up to  $\sim 10^4 \text{ K}$ , driving thermal mass loss via hydrodynamic escape (Yelle et al. 2008; Murray-Clay et al. 2009; Sanz-Forcada et al. 2011; Owen & Jackson 2012). On highly irradiated giant planets, the outflow may be sufficiently rapid that heavy elements are dragged along via collisions with hydrogen (Vidal-Madjar et al. 2004; Linsky et al. 2010; Koskinen et al. 2013; Ballester & Ben-Jaffel 2015). EUV-driven hydrodynamic escape is particularly relevant for close-orbiting super-Earth- to Neptune-sized planets, potentially leading to complete evaporation of their gaseous envelopes on gigayear timescales, while Jupiter-sized planets are more likely to retain their envelope over these timescales (Owen & Jackson 2012; Owen & Wu 2016; Fossati et al. 2017).

### 1.2. Stellar UV Effects on Atmospheric Chemistry of Sub-Neptune Planets

UV radiation also directly affects the observable features of sub-Neptune exoplanetary atmospheres. For example, atmospheric transmission spectra of GJ 1214b with the Hubble Space Telescope (HST) Wide Field Camera 3 have revealed a “flat” transmission spectrum from  $\sim 0.78\text{--}1.7 \mu\text{m}$ ; that is, the spectrum is missing the strong absorption features expected from  $\text{H}_2\text{O}$  and other molecules (Bean et al. 2010; Berta et al. 2012). Kreidberg et al. (2014) concluded that the spectrum is inconsistent with a high molecular weight (>50%  $\text{H}_2\text{O}$ ) atmosphere, arguing that the featureless spectrum is likely a result of optically thick clouds or photochemical hazes, whose formation is catalyzed by UV radiation. For sub- to super-Earth planets with temperatures  $\lesssim 700 \text{ K}$ , the dominant elemental reservoirs are  $\text{H}_2\text{O}$ ,  $\text{NH}_3$ , and  $\text{CH}_4$  (Burrows & Orton 2010; Madhusudhan et al. 2016; Fortney et al. 2021). UV radiation from a planet’s host star penetrates the upper atmosphere, photodissociating  $\text{CH}_4$ , and initiates photochemical reactions leading to the formation of opaque organic molecules, which can cause features such as the observed flat transmission spectrum of GJ 1214b (Miller-Ricci Kempton et al. 2012; Arney et al. 2017; Linsky 2019).

Remote sensing of exoplanet habitability relies heavily on the detection of gaseous biosignatures, particularly  $\text{O}_2$ ,  $\text{O}_3$ ,  $\text{CO}$ , and  $\text{CH}_4$ , but also including other hydrocarbons and  $\text{N}$  and  $\text{S}$  based gases (Des Marais et al. 2002; Segura et al. 2005; see Schwieterman et al. 2018 for a more extensive overview of gaseous biosignatures). Molecular oxygen and ozone are

readily detectable in the near-UV (NUV;  $\sim 1700\text{--}3200 \text{ \AA}$ ), visible, and mid-IR and have the potential to be strong indicators of biological activity. On Earth,  $\text{O}_3$  is a byproduct of the photolysis of  $\text{O}_2$ , which is almost entirely sourced via oxygenic photosynthesis (Des Marais et al. 2002; Kiang et al. 2007). However, EUV and far-UV (FUV;  $\sim 912\text{--}1700 \text{ \AA}$ ) radiation shortward of  $\sim 1700 \text{ \AA}$ —especially in the  $\text{Ly}\alpha$  emission line, which can comprise  $\sim 37\%\text{--}75\%$  of the total FUV flux for M dwarfs (France et al. 2013)—heavily influence oxygen chemistry, photodissociating  $\text{CO}_2$  and  $\text{H}_2\text{O}$ , and leading to escape of  $\text{H}$  and buildup of  $\text{O}$  and  $\text{O}_2$  (Hu et al. 2012; Burkholder et al. 2015; Gao et al. 2015). The balance of oxygen and ozone in the atmosphere can be at least partially described by the Chapman mechanism (Chapman 1930), in which  $\text{O}_2$  is photodissociated by FUV photons, which recombine to form  $\text{O}_3$ , and  $\text{O}_3$  is in turn photodissociated by NUV and blue-optical photons, resulting in the production of  $\text{O}_2$ . Thus, the ratio of stellar FUV to NUV flux becomes critical for oxygen chemistry in the atmosphere; if a host star produces a large amount of FUV and relatively little NUV flux, a substantial  $\text{O}_3$  atmosphere may arise entirely via photochemical processes (Segura et al. 2010; Hu et al. 2012; Domagal-Goldman et al. 2014; Tian et al. 2014; Gao et al. 2015; Schwieterman et al. 2018).

### 1.3. UV Time Variability of Cool Stars

Variability of UV radiation from a host star is critical to photochemistry and atmospheric stability of exoplanets. Solar EUV flux varies by factors up to  $\sim 100$  on minute timescales during intense flares (Woods et al. 2012). In G-, K-, and M stars, quiescent FUV radiation is emission line dominated, but continuum emission can become the dominant UV luminosity source during stellar flares (Kowalski et al. 2010; Loyd et al. 2018). M and K dwarfs in particular exhibit regular flare activity, even in old and inactive stars, and the energy released during these events may account for more FUV flux than the quiescent emission over stellar lifetimes (Loyd et al. 2018; France et al. 2020b). Knowledge of stellar flare rates and energies is therefore necessary to allow for estimates of lifetime-integrated UV flux experienced by exoplanets, especially those being assessed for their potential habitability. Solar observations have shown that many high-energy flaring events are associated with an accompanying coronal mass ejection (CME) and that larger flare fluxes result in larger CME masses (Munro et al. 1979; Aarnio et al. 2011). These CMEs result in highly energetic accelerated particles that impact planetary atmospheres, significantly enhancing pickup ions and leading to dramatic increases in atmospheric escape rate (Lammer et al. 2007; Jakosky et al. 2015; Airapetian et al. 2017). Furthermore, it has been shown that energetic particle deposition into the atmospheres of terrestrial planets can lead to significant changes in observable atmospheric oxygen abundances (Segura et al. 2010; Tilley et al. 2019).

### 1.4. The MUSCLES and Mega-MUSCLES Treasury Surveys

With the growth of exoplanetary science and the associated awareness of the importance of the host star’s UV radiation field on the evolution of exoplanetary atmospheres, the community resources devoted to UV characterization of cool stars have increased (Shkolnik et al. 2016; France et al. 2018; Duvvuri et al. 2023). This is particularly important since it has

**Table 1**  
List of Targets

Star	Sp. Type	$T_{\text{eff}}$ (K)	Distance (pc)	Mass ( $M_{\odot}$ )	Radius ( $R_{\odot}$ )	No. of Planets <sup>a</sup>
WASP-17	F4	6548	405.0 $_{-8.4}^{+8.8}$	1.57 $\pm$ 0.092	1.31 $\pm$ 0.03	1
HD 149026	G0	6084	75.0 $\pm$ 1.7	1.46 $\pm$ 0.08	1.34 $\pm$ 0.02	1
WASP-127	G5	5828	159.0 $\pm$ 1.2	1.31 $\pm$ 0.05	1.33 $\pm$ 0.03	1
WASP-77A	G8	5605	105.2 $\pm$ 1.2	1.00 $\pm$ 0.05	0.96 $\pm$ 0.02	1
TOI-193	G7	5443	80.4 $\pm$ 0.3	1.02 $_{-0.03}^{+0.02}$	0.95 $\pm$ 0.01	1
HAT-P-26	K1	5062	141.8 $_{-1.1}^{+1.2}$	0.82 $\pm$ 0.03	0.79 $_{-0.04}^{+0.10}$	1
HAT-P-12	K5	4653	142.8 $\pm$ 0.5	0.73 $\pm$ 0.02	0.70 $_{-0.01}^{+0.02}$	1
WASP-43	K7	4124	86.7 $\pm$ 0.3	0.72 $\pm$ 0.03	0.67 $\pm$ 0.01	1
L 678-39	M2.5	3490	9.4 $\pm$ 0.01	0.34 $\pm$ 0.01	0.34 $\pm$ 0.02	3
L 98-59	M3	3429	10.6 $\pm$ 0.003	0.31 $\pm$ 0.01	0.31 $\pm$ 0.01	4
LP 791-18	M6	2949	26.5 $\pm$ 0.06	0.14 $\pm$ 0.01	0.17 $\pm$ 0.02	3

**Note.**

<sup>a</sup> Sourced from NASA Exoplanet Archive. We report only the number of confirmed exoplanets.

**References.** From top to bottom: (1) Anderson et al. (2010); (2) Sato et al. (2005); (3) Lam et al. (2017); (4) Maxted et al. (2013); (5) Jenkins et al. (2020); (6) Hartman et al. (2011); (7) Hartman et al. (2009); (8) Hellier et al. (2011); (9) Luque et al. (2019); (10) Kostov et al. (2019); (11) Crossfield et al. (2019). References represent the announcement of discovery of the exoplanet(s). Further references are listed in the more detailed system descriptions in Appendix A.

been shown that empirical scaling relations alone are insufficient to model the evolution of planetary atmospheres, and the extended UV continuum and UV emission lines are necessary to generate accurate models (Peacock et al. 2022; Teal et al. 2022). The MUSCLES Treasury Survey (HST Cycle 22; PI—France) began to address this dearth of observations by creating panchromatic 5 Å–5.5 μm spectral energy distributions (SEDs) of M and K dwarfs, which have since been used extensively to study the importance of the UV radiation environment on exoplanets (for example, Kawashima & Ikoma 2018; Lora et al. 2018; Chen et al. 2021). The MUSCLES SEDs consist of observational spectra in the X-ray (5–50 Å: XMM-Newton and Chandra X-ray Observatory) and UV (1170–5700 Å: HST), empirical estimates of the EUV (100–1170 Å), which cannot be presently observed owing to lack of an operating EUV observational facility (France et al. 2022), and stellar atmospheric models of the IR (5700 Å–5.5 μm; Loyd et al. 2016). Stars in the MUSCLES survey covered a range of spectral types from K1V—M5V, and all but one were considered “optically inactive” due to having H $\alpha$  in absorption. Despite this classification, all showed chromospheric and coronal activity (France et al. 2016; Loyd et al. 2016; Youngblood et al. 2016).

The MUSCLES survey was subsequently expanded to include an additional 13 M dwarfs in the Mega-MUSCLES survey (HST Cycle 25; PI—Froning). Mega-MUSCLES has a particular focus on low-mass ( $M < 0.3 M_{\odot}$ ) stars with a range of spectral types from M0–M8, including Barnard’s star and TRAPPIST-1. Mega-MUSCLES observations revealed a number of UV and X-ray flares on stars with a range of activity levels (Froning et al. 2019; France et al. 2020b), demonstrating that optical activity indicators are poor predictors of the high energy variability of cool stars and further reinforcing the need for direct UV and X-ray observations of specific planet-hosting stars.

### 1.5. The MUSCLES Extension for Atmospheric Spectroscopy

The recent launch of JWST has begun an unprecedented era in exoplanetary atmospheric characterization. Atmospheric spectroscopy of exoplanets ranging from Earth-sized terrestrial planets

through giant hot-Jupiters are currently being obtained via the JWST Early Release Science (ERS) and Guaranteed Time Observations (GTO) programs. As described above, the high-energy SEDs of the host stars will be crucial to accurately interpret the results of these spectroscopic observations. We have identified 11 JWST guaranteed time targets that have no previous UV observations in the HST archive. In this work, we present the MUSCLES Extension for Atmospheric Transmission Spectroscopy, which extends the original MUSCLES survey over a larger range in stellar mass to include these 11 previously uncharacterized stars. The stars in this work range from M6–F4 and host planets ranging from super-Earths to hot-Jupiters. We expand on the methods of the MUSCLES survey and create panchromatic SEDs of these stars, characterize them in relation to other known planet and non-planet-hosting stars, and address selective bias toward observing low-activity stars, which may impact our interpretations of observed exoplanetary atmospheres.

We structure the paper as follows: Section 2 describes the observational campaign, including HST, Chandra, and XMM-Newton observations, and the methods used to reconstruct the currently unobservable regions in the EUV. In Section 3 we show the results of our observations and put them in context relative to the broader population of stellar surveys. We also discuss the importance of studying the time variability of host stars, motivated by the detection of two X-ray flares in the star L 98-59. Finally, we summarize the main results of this work in Section 4. A list of observed targets including particular observation details, SED construction, and descriptions of planetary systems can be found in Appendix A. Lists of UV emission line fluxes can be found in Appendix B.

## 2. Observations

Observational data were obtained from HST, Chandra, and XMM-Newton. All HST observations were obtained through a dedicated observing program for this survey (HST Cycle 28, program ID 16166; PI—France), while Chandra and XMM-Newton were a combination of new and archived observations. In Table 1 we present a brief overview of each target in the MUSCLES Extension in order of decreasing effective temperature. For a detailed description of the planetary systems and



their relation to the JWST ERS and GTO programs, as well as X-ray and UV data quality, major emission characteristics, and details of X-ray/FUV proxy stars (see Section 2.3), we refer the reader to Appendix A.

### 2.1. FUV and NUV

Unless otherwise stated, we refer to FUV as  $912 \text{ \AA} < \lambda < 1700 \text{ \AA}$  and NUV as  $1700 \text{ \AA} < \lambda < 3200 \text{ \AA}$ . We employed the STIS G140L and G230L gratings for the FUV and NUV continuum and emission lines, respectively, and the G140M grating for higher-resolution spectra in the Ly $\alpha$  emission region. Finally, in order to calibrate the UV data to visible/IR photospheric models and ground-based spectra, we obtained optical observations using the STIS G430L grating. The exposure times were estimated based on the minimum amount of time required to achieve signal-to-noise ratio (S/N) of  $\simeq 10$  per resolution element in the characteristic line and continuum regions: Ly $\alpha$  (STIS G140M,  $\lambda = 1216.0 \text{ \AA}$ ), C II (STIS G140L), and NUV continuum (STIS G230L,  $\lambda = 2820 \text{ \AA}$ , longward of Mg II), and  $S/N > 20$  in the optical regions. We create simulated spectra for exposure time estimates by taking stars of similar spectral types from the HST archive (Procyon,  $\alpha$  Cen A,  $\epsilon$  Eri, HD 85512, and GJ 832), scaled to the V magnitude of the target star and use the STScI exposure time calculator<sup>8</sup> to estimate the minimum exposure time. As we shall discuss in Section 3, the MUSCLES Extension targets were lower activity than expected, and the S/N in the FUV was lower than that calculated in the observation proposal. In the NUV/optical, the S/N calculations were accurate with  $S/N > 20$  per resolution element. In total, our HST spectra typically span  $\sim 1150\text{--}5500 \text{ \AA}$ .

For some cool stars of spectral type K5 and later, the required exposure time to obtain an adequate S/N was prohibitively long, and we opted to exclude G140L and G140M observations. We were thus unable to acquire direct FUV emission line measurements for these targets. This includes HAT-P-12, LP 791-18, and WASP-43.

L 678-39 exceeded the STIS G140L bright object protection limits, and we thus utilized the HST Cosmic Origins Spectrograph (COS) G130M (selecting the  $\lambda 1222$  CENWAVE to avoid specific bright emission lines) and G160M modes, rather than STIS. For similar reasons, we have observed HD 149026 with STIS E230M rather than G230L.

We reduced the HST data as follows:

First, we examined all observations for pointing or data quality errors. Several observations (G140M: HD 149026, L 98-59, TOI-193; G140L: WASP-17; G230L: LP 791-18) had incorrect extraction regions during the X1DCORR routine, presumably due to low signal. We examined the flat fielded images to determine proper extraction regions and re-extracted them manually using the Python package *stistools*.<sup>9</sup> We also found poor data quality flags on the blue end of the G430L CCD for all observations, typically spanning  $\sim 100$  pixels; these were mostly pixels that were flagged for having zero flux (i.e., flag 16384 in the data quality array; see Section 2.5 of Sohn et al. 2019). The FUV MAMA detectors did not show any serious data quality issues.

After screening the observations and removing portions with poor data quality, we proceeded to coadd the spectra for any

target that had multiple observations with the same grating. We first interpolated each spectrum onto a common wavelength grid with  $\Delta\lambda = 0.5 \text{ \AA}$ , oversampling the native resolution of the gratings. This process conserves the total observed flux while allowing us to perform a simple coaddition. We then performed a coaddition of the spectra using an exposure time-weighted average.

After performing the coaddition for each grating observation, we examined the final S/N of each and culled data that we considered to be of poor quality; we chose a threshold of  $S/N > 3$  per pixel for data to be usable in the final spectrum. This resulted in all of the continua of all G140L observations having too low S/Ns to include in the final spectra, although we do find emission lines above the S/N threshold for most targets. G230L spectra were typically low S/N on the blue end until  $\sim 2000\text{--}2300 \text{ \AA}$ , depending on effective temperature, at which point the photospheric emission begins to pick up. G430L spectra were all above the S/N threshold after culling the poor data quality pixels on the blue end of the detector. Finally, we compare the reported stellar  $B - V$  color to a table of unreddened colors of the appropriate spectral type to determine if a dereddening procedure is required to account for interstellar extinction. We found  $A_v < 0.1$  for all targets and thus do not account for reddening in any of the analysis.

After cleaning and coadding the spectra, we measured the emission line fluxes of the seven lines listed in Table 6.

For emission lines with S/N greater than the threshold, the reported flux is the numerically integrated flux over the continuum-subtracted line region:

$$F_{\text{ion}} = \int_{\lambda_0 - \delta\lambda}^{\lambda_0 + \delta\lambda} F(\lambda) d\lambda \quad (1)$$

where  $F(\lambda)$  is the continuum-subtracted flux density. The continuum flux density is estimated from a polynomial fit to the continuum on either side of the emission line. The integration width,  $\delta\lambda$ , was selected by hand for each line to accommodate varying line widths and was typically  $2.5 \text{ \AA}$  for the low-resolution G140L spectra.

For targets with emission line fluxes below the S/N threshold, we report the rms value of the flux density over the continuum-subtracted line region as an upper limit on the emission line flux.

### 2.2. X-Ray Data

The MUSCLES Extension included X-ray data of four stars via Chandra observations and seven via XMM-Newton observations. The data were a combination of new observations obtained for this program as well as archival observations. The new XMM-Newton observations of WASP-43 and L 98-59 were taken concurrently with the UV observations obtained in this work. Source X-ray spectra were extracted from a circular region with a  $2''.5$  radius around the proper-motion corrected source location and an annular background region centered on the target location encompassing as much area as possible without including other sources. Some targets were close to the edge of the detector chip, and a background region centered on the target would extend beyond the edges of the chip; in these cases, we used a circular background region from a nearby representative area. Chandra data were analyzed using the Chandra Interactive Analysis of Observations (CIAO; Fruscione et al. 2006) software. We use the CIAO *dmlist* routine to

<sup>8</sup> <https://etc.stsci.edu/etc/input/stis/spectroscopic/>

<sup>9</sup> <https://stistools.readthedocs.io/en/latest/>

obtain background-subtracted count rates. For XMM-Newton observations, we use the Scientific Analysis System (SAS 20.0.0; Gabriel et al. 2004) with the standard procedure and filters. Photon events were limited to those with an energy range of 0.3–10 keV to remove spurious high-energy particle events. Each target was screened for both source and background flaring. Background flares are common in XMM-Newton observations and were removed from several targets. L 98-59 is the only target that showed a source flaring event. Flares occurred in both observations of L 98-59, which continued throughout the duration of each exposure. These flares are discussed in detail in Section 3.5.

Five targets were successfully detected at the  $3\sigma$  level; however, the number of counts remaining in the source regions were insufficient to allow robust spectral modeling. Three of four observations with the Chandra ACIS-S detector and three of eight observations with the XMM-Newton EPIC pn detector were nondetections at the  $3\sigma$  level. To estimate a flux for each target, we use the PIMMS<sup>10</sup> tool, assuming a thermal plasma model with a temperature of 0.43 keV and a hydrogen column density estimated based on stellar distance using the relations from Wood et al. (2005). For detected sources we input the observed count rate. For nondetected sources we input a theoretical count rate, which would produce a  $3\sigma$  detection given our exposure time and report the estimated flux as an upper limit. X-ray sources and their corresponding references are compiled in Table 2 and Table 3.

### 2.3. X-Ray and FUV Proxy Spectra

Due to the amount of X-ray nondetections and the low S/N of our G140L observations, we opted to use scaled proxy spectra to represent the X-ray ( $\sim 5$ –100 Å) and FUV continuum. Proxy stars were chosen to have similar spectral type, age, and activity levels, based on effective temperature, rotation period, and  $\log R'_{\text{HK}}$ . Spectra for the proxy stars were obtained from the publicly available MUSCLES (France et al. 2016) archives. The MUSCLES spectra used the HST COS to obtain UV measurements down to  $\sim 1150$  Å, and a combination of XMM-Newton and Chandra observations and Astrophysical Plasma Emission Code (APEC; Smith et al. 2001) models for the X-rays. After selecting a suitable proxy star, the proxy spectrum was scaled to the blue end of the NUV spectrum (G230L) via a least-squares fitting method minimizing the quantity  $((F_{\text{ref}} - \alpha \times F_{\text{proxy}})/\sigma_{\text{ref}})^2$  where  $F_{\text{ref}}$  represents the G230L flux of the MUSCLES Extension target,  $F_{\text{proxy}}$  is the flux of the proxy spectrum,  $\alpha$  is the non-wavelength-dependent scaling factor applied to the proxy spectrum, and  $\sigma_{\text{ref}}$  is the  $1\sigma$  error of the observed G230L spectrum. We applied this routine to a region approximately 100 Å wide where the proxy spectrum overlaps with the blue end of the observed G230L spectrum. The continua of the scaled proxy spectra match the continua of the observed STIS spectra within the  $1\sigma$  uncertainty of the STIS data. Considering the importance of UV emission lines in atmospheric modeling, we replace the emission lines of the proxy spectra with the measured emission lines from our MUSCLES Extension observations where possible; this provides the best balance between a representative continuum and ground-truth emission line fluxes. In regions where our observed emission lines exceed the S/N  $> 3$  per pixel threshold, we remove the proxy spectrum

and replace it directly with our observed data. Regions that include the observed emission lines are recorded in the instrument data column of the final SED data products, represented by a bit value corresponding to the instrument and grating with which the line was measured (Section 2.7). For lines that are below the S/N threshold, we first construct a representative line by assuming a Gaussian emission with a width of  $60 \text{ km s}^{-1}$  for M stars and  $70 \text{ km s}^{-1}$  for all others, based on France et al. (2020b) and France et al. (2010), and match the total integrated flux. We then replace the emission line region in the proxy spectrum with the constructed flux-matched emission line. Proxy spectra are used in the regions of 5–100 Å and again from 1170 Å to the beginning of the high-S/N NUV observations, which ranges from 1750–2600 Å. The FUV proxy region excludes the reconstructed Ly $\alpha$  range from  $\sim 1212$ –1220 Å.

### 2.4. Ly $\alpha$

The Ly $\alpha$  emission line is heavily attenuated by neutral hydrogen in the interstellar medium (ISM), with the core of the line often being unobservable for even the nearest stars, leaving only the wings of the line observed. Ly $\alpha$  flux plays an important role in the photochemistry of exoplanet atmospheres, and therefore it is crucial to properly reconstruct the intrinsic line profile in order to accurately model atmospheric chemistry (Miguel et al. 2015; Arney et al. 2017). We follow the approach of Youngblood et al. (2022) to reconstruct the intrinsic Ly $\alpha$  profile from the ISM-attenuated, observed spectra of the stars with good S/N G140M data. We simultaneously fit a model of the intrinsic profile and the ISM absorption to the observed line wings. The functional form of the intrinsic line profile is a Voigt emission profile with a self-reversal that follows the shape of the emission:

$$F_{\text{emission}}^{\lambda} = \mathcal{V}^{\lambda} \cdot \exp(-p\mathcal{V}_{\text{norm}}^{\lambda}) \quad (2)$$

where  $\mathcal{V}^{\lambda}$  is the Voigt emission profile,  $p$  is the self-reversal parameter, and  $\mathcal{V}_{\text{norm}}^{\lambda}$  is the peak-normalized Voigt profile. The self-reversal parameter is allowed to vary between 0 and 3. Larger values of  $p$  result in a deeper self-reversal profile.

The ISM absorption is modeled as two Voigt profiles without self-reversal parameters: one for hydrogen and one for deuterium.

We use the reconstructed line for the region of  $\sim 1212$ –1220 Å in the final SEDs. For targets where G140M observations were not feasible or the S/N was insufficient to fit with the Markov Chain Monte Carlo (MCMC) method, we estimated the total Ly $\alpha$  flux by using a power-law relation to the total Mg II  $\lambda\lambda 2799, 2803$  Å surface flux (Wood et al. 2005; Youngblood et al. 2016). After estimating the Ly $\alpha$  flux based on the Mg II relation, we create a line profile of the form given by Equation (2) by selecting a fixed self-reversal parameter and iterating through a range of amplitudes until the integrated flux of the self-reversed Voigt profile matches the flux estimated by the Mg II relation. The self-reversal parameter was chosen to be 1.5 for M type stars, 2.0 for K, and 2.4 for G and F types based on the results from Youngblood et al. (2022). The integrated Ly $\alpha$  flux of the Voigt profiles matches the estimated flux to within 0.05%.

Figure 1 shows a reconstructed profile for two stars; HD 149026, for which the G140M observation was sufficient to fit with the MCMC method, and WASP-77A, for which we used the Mg II flux estimation. The WASP-77A spectrum exhibits both large negative fluxes and a spurious peak toward the line

<sup>10</sup> The Portable Interactive Multi-Mission Simulator, <https://cxc.harvard.edu/toolkit/pimms.jsp>.

center; this is a result of poor background subtraction of geocoronal Ly $\alpha$ .

### 2.5. Visible through IR

The G430L spectra extend into visible wavelengths up to 5700 Å. After this point, we use the BT-Settl stellar atmosphere models (Allard et al. 2011) to extend the SEDs into the IR up to 5.5  $\mu$ m. The BT-Settl models cover a grid of effective temperatures ( $T_{\text{eff}}$ ) and surface gravity ( $\log g$ ) and provide a flux observed at Earth based on stellar radius and distance. We scale the BT-Settl model to the NUV spectra from G430L as described below.

First, we convolve the high-resolution BT-Settl model to match the resolution of the G430L data. We then take region  $>5000$  Å where the BT-Settl model overlaps with the G430L spectrum and scale the model using the same least-squares method described in Section 2.3. The fits were examined by eye and found to be well representative of the shape of the observed spectra. Figure 2 shows the BT-Settl atmospheric model for  $6000 \text{ K} < T_{\text{eff}} < 6100 \text{ K}$  and  $4.0 < \log g < 4.5$  scaled to the G430L spectrum of the G0 star HD 149026 using this method.

### 2.6. EUV Estimations

The EUV is heavily attenuated by the ISM, particularly in the Lyman continuum region from the photoionization point of H at 912 Å down to  $\sim 400$  Å. Interstellar extinction, combined with the lack of an operating EUV observatory, means we currently do not have the ability to observe the EUV spectra of stars other than the Sun, and the HST sensitivity drops sharply below  $\sim 1170$  Å; we therefore present estimations of the EUV flux from 100–1170 Å. The EUV spectrum is estimated in nine bandpasses from 912–1170 Å using empirically derived relations between total Ly $\alpha$  flux and EUV flux from Linsky et al. (2014). Linsky et al. (2014) used a combination of solar models ( $\lambda < 2000$  Å) and direct observations, utilizing the Far Ultraviolet Spectroscopic Explorer (912–1170 Å) and the Extreme Ultraviolet Explorer (100–400 Å), to show that the ratio of EUV to Ly $\alpha$  flux varies slowly with the total Ly $\alpha$  flux. They established direct ratios of  $F(\Delta\lambda)/F(\text{Ly}\alpha)$ , where  $\Delta\lambda$  is the wavelength region of the  $\sim 100$  Å bandpass, and both  $F(\Delta\lambda)$  and  $F(\text{Ly}\alpha)$  are scaled to 1 au. After calculating the EUV flux in the bandpass, we re-scale the flux to the appropriate stellar distance.

### 2.7. Panchromatic Spectrum Assembly

With all of the data products described above in hand, we developed a procedure for stitching the spectra together into a continuous panchromatic spectrum. We first define a prioritization order for the spectral segments, placing the highest priority on direct observations with good S/N, followed by Ly $\alpha$  reconstructions and EUV estimations, and finally scaled proxy and BT-Settl spectra.

Keeping in mind our goal of using direct observations wherever possible, we opted not to perform any optimization routine to determine the location of the join. Instead, we directly inserted whichever data product was highest on the priority list for the given wavelength range. This occasionally results in a small jump discontinuity at the joining location. We investigated these discontinuities by fitting a smooth spline between the two regions and finding the total amount of “missing” flux, which was  $< 0.7\%$  of the flux over the same

region without including a smooth join. We therefore consider the discontinuities to be negligible and do not attempt to correct them. In cases where two direct observations overlap, we give priority to whichever observation has higher S/N over the region in question.

Figure 3 shows all of the final panchromatic SEDs.

The MUSCLES Extension SEDs are available as high-level science products on the MUSCLES portal hosted on the Mikulski Archive for Space Telescopes (MAST) archive<sup>11</sup> as an FITS file containing a PrimaryHDU with general observation information and a BinTableHDU containing the spectral data. We provide two versions of each SED: one that retains the native instrument or model resolutions, and one that is rebinned to a constant 1 Å resolution. Each panchromatic SED provides the following information:

1. Bin: midpoint and edges of the wavelength bins in [Å].
2. Flux density: measurement and error of the flux density in [ $\text{erg s}^{-1} \text{cm}^{-2} \text{Å}^{-1}$ ] as well as the value normalized by the bolometric flux [ $\text{Å}^{-1}$ ].
3. Exposure: MJD of the beginning of the first contributing exposure, the end of the last contributing exposure, and the cumulative exposure time [s].
4. Normalization: any normalization factor applied to flux bin.
5. Instrument: a bit-wise flag identifying the source of the flux data for the bin. Note that for binned spectra, we may have combined adjacent bins from different sources. This is accounted for in the bit-wise instrument flag by adding the bit value for each of the respective instruments.

## 3. Results

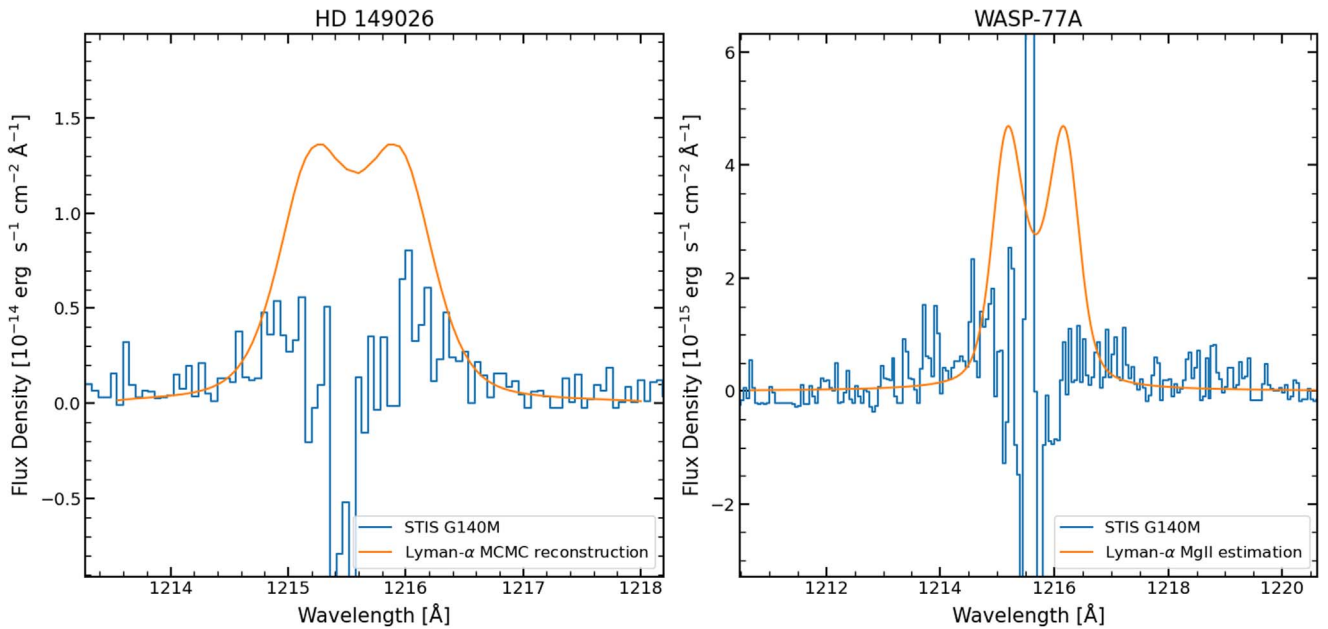
France et al. (2018) showed that exoplanet-hosting stars selected from RV and transit methods exhibit lower UV activity than the general field population. In order to further understand the potential effects of selecting stars chosen from planet detection surveys to use as templates for atmospheric modeling, we present a comparison of our targets to previously studied planet-hosting and “non-planet-hosting” stars. We examine first the fractional X-ray luminosity (Section 3.1), which is an indicator of coronal activity levels, then the FUV/NUV flux ratio and fractional UV emission line luminosities (Sections 3.2 and 3.3), which are indicative of chromospheric/transition-region activity levels, and finally the UV flux environment experienced by the planets orbiting our target stars compared to those in the MUSCLES survey (Section 3.4). The X-ray flaring events of L 98-59 are discussed in Section 3.5.

### 3.1. X-Ray Flux

The fraction of stellar bolometric flux emitted in the X-ray band has been shown to be correlated with chromospheric and coronal activity indicators such as rotation period,  $R'_{\text{HK}}$ , and  $R_{\text{H}\alpha}$ , and thus is a useful measure of stellar activity levels (Katsova & Livshits 2011; He et al. 2019; Kostov et al. 2019; Linsky et al. 2020). Figure 4 shows the fractional X-ray luminosity of MUSCLES Extension stars compared to a large survey by Wright et al. (2011, 2018). Wright et al. (2011) observed 824 solar and late-type stars to study the relation between rotation period and stellar activity; they extended this

<sup>11</sup> doi:10.17909/T9DG6F.





**Figure 1.** Left: Ly $\alpha$  reconstruction for HD 149026 using the Youngblood et al. (2022) MCMC method. Right: Ly $\alpha$  reconstruction for WASP-77A using the Mg II flux estimation method.

survey in Wright et al. (2018) to include a sample of 19 fully convective M dwarfs.

Here we use the X-ray flux or upper limits from PIMMS as described in Section 2.2 and define the bolometric flux based on effective temperature:

$$F_{\text{bol}} = \sigma T_{\text{eff}}^4 \left( \frac{R_*}{d} \right)^2 \quad (3)$$

where  $\sigma$  is the Stefan–Boltzman constant,  $R_*$  is the stellar radius, and  $d$  the stellar distance. Using this definition of bolometric flux allows for consistency between measurements of our own targets as well as to those of France et al. (2018), who use the same definition. Results from the PIMMS analysis are listed in Tables 2 and 3.

Young, rapidly rotating stars show a saturation at  $\log L_x/L_{\text{bol}} \sim -3$ , and older stars begin to show a sharp decline in fractional X-ray luminosity after reaching rotation periods of a few days (Wright et al. 2011; Astudillo-Defru et al. 2017). Here, we take “active” stars to be broadly defined as those with  $-5 \lesssim \log L_x/L_{\text{bol}} \lesssim -3$  and “inactive” as those with  $\log L_x/L_{\text{bol}} < -5$  (Linsky 2019, and references therein). Under this definition, we find that nine of the 11 stars from this work exhibit low fractional X-ray luminosities consistent with low coronal activity. Note that the X-ray flare of L 98-59, indicated by the black square in Figure 4, pushes the star into the active regime, highlighting the importance of taking into account stellar variability, as we discuss in Section 3.5.

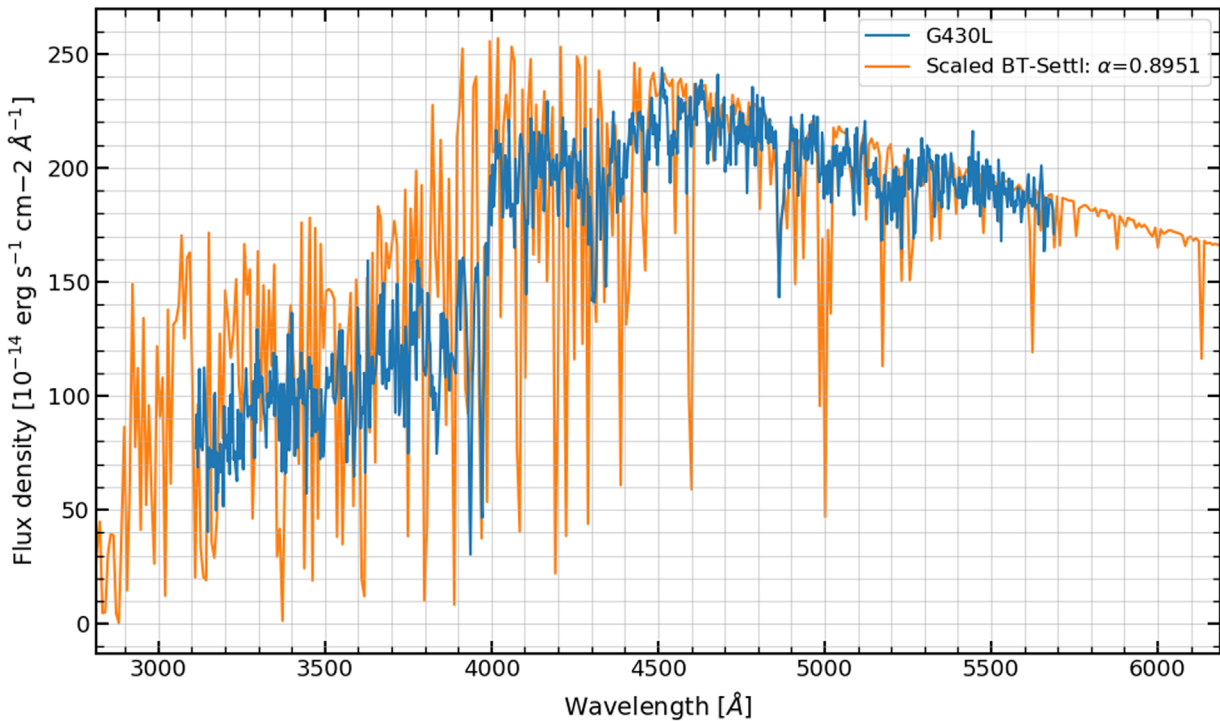
### 3.2. FUV to NUV Flux Ratios

The FUV to NUV flux ratio is an important measure for exoplanet habitability studies. As described in Section 1.2, the FUV/NUV ratio can impact atmospheric oxygen chemistry via the Chapman reactions. However, for a star with a large FUV/NUV flux ratio, destruction of  $\text{O}_3$  via NUV flux may not balance its creation from FUV flux, leading to an abiotic buildup of ozone and the detection of a potential false-alarm

biosignature (Segura et al. 2010; Domagal-Goldman et al. 2014; Schwieterman et al. 2018).

While a larger fraction of the NUV is contributed by the stellar photosphere, the FUV/NUV ratio can also be thought of as a chromospheric activity indicator, as most of the stellar FUV flux from GKM stars comes from emission lines as a result of stellar activity rather than continuum emission. It is important to keep in mind, however, that this ratio is strongly correlated with effective temperature. As  $T_{\text{eff}}$  increases, the photospheric emission of the star begins to push farther into the NUV region, decreasing the FUV/NUV ratio. There is a minimum in the FUV/NUV ratio at  $\sim 1 M_{\odot}$  after the photospheric emission begins to push all the way into the FUV, resulting in an increase of FUV/NUV flux, as shown in Figure 5. This makes the FUV/NUV ratio less accurate as an activity indicator for hotter stars without subtracting the photospheric contribution. However, at a given stellar mass, the FUV/NUV ratio is a measure of the excess FUV emission contributed by chromospheric and transition-region activity.

To put the MUSCLES Extension stars in context with the general stellar population, we compare them to the HAZMAT III (Schneider & Shkolnik 2018) and HAZMAT V (Richey-Yowell et al. 2019) surveys. Comparison to the HAZMAT study offers an opportunity to compare stars selectively chosen as exoplanet hosts (MUSCLES Extension) to a nonselective field survey (HAZMAT). The HAZMAT III and HAZMAT V surveys present studies of 642 M dwarfs and 455 K dwarfs, respectively. Figure 6 shows the FUV/NUV flux ratio in the GALEX bandpasses (FUV: 1350–1750 Å, NUV: 1750–2800 Å) of the MUSCLES Extension stars compared to the two HAZMAT surveys, which have been grouped to 10 stellar mass bins and separated by age, with “old” stars being those with an age of  $\sim 5$  Gyr (see Figure 12 of Richey-Yowell et al. 2019). We performed a linear fit using a least-squares routine to fit the stars between  $0.2$  and  $0.85 M_{\odot}$ . The bounds of the fit exclude stars in the saturated FUV/NUV regime of  $\sim 2 \times 10^{-1}$  at  $M < 0.2 M_{\odot}$ , as well as the MUSCLES Extension stars with spectral type of F or G for consistency with



**Figure 2.** Result of the HD 149026 BT-Settl scaling routine plotted with the STIS G430L spectrum. The BT-Settl stellar atmosphere model is convolved to G430L resolution and scaled by a factor of  $\alpha = 0.8951$ .

the HAZMAT surveys, which include only M and K dwarfs. The slopes of the linear fits are consistent within the  $1\sigma$  level:  $-2.54 \pm 0.2$  for HAZMAT stars and  $-2.36 \pm 0.5$  for MUSCLES Extension stars. However, the MUSCLES Extension stars are considerably less FUV luminous than the HAZMAT stars, offset in their FUV/NUV ratio by  $\sim 3\sigma$ , suggesting that the MUSCLES Extension targets have significantly less FUV activity than the average populations of old K and M dwarfs in the field. This can be explained by a selection bias from the techniques used to detect exoplanet systems. RV and transit surveys largely select for low-activity stars, as active stars add excess noise to RV and transit measurements, which can be mistaken for planetary signals (Butler et al. 2017).

### 3.3. UV Ion Ratios

We quantify chromospheric and transition-region activity via the fraction of bolometric luminosity,  $L_{\text{ion}}/L_{\text{bol}}$ , for C II ( $\lambda\lambda$  1334.5, 1335.6 Å) and Si IV ( $\lambda\lambda$  1393.8, 1402.8 Å). Figure 7 shows the MUSCLES Extension targets plotted against both planet- and non-planet-hosting stars from the France et al. (2018) survey.

The histograms of bolometric luminosity ratios for planet and non-planet-hosting stars suggest two different populations. Means and standard deviations for both populations are listed in Table 4. We apply a two-sided Kolmogorov–Smirnov (K-S) test to the following groups: (1) All non-planet-hosting stars and all planet-hosting stars, (2) non-planet-hosting stars and MUSCLES Extension stars, (3) MUSCLES Extension stars and France et al. (2018) planet-hosting stars. The K-S test is applied with the null hypothesis that the two sample groups come from the same parent distribution and the alternative that they have differing distributions. We find that the populations of non-planet hosts and planet hosts for both groups 1 and 2 differ at

the  $3\sigma$  level or greater for C II and Si IV, indicating that stars chosen from exoplanet surveys have statistically different activity levels than the general population. We do not reject the null hypothesis that MUSCLES Extension stars come from the same distribution than the France et al. (2018) planet-hosting stars, suggesting that the MUSCLES Extension targets are similar in activity level to the other planet-hosting stars in our test.

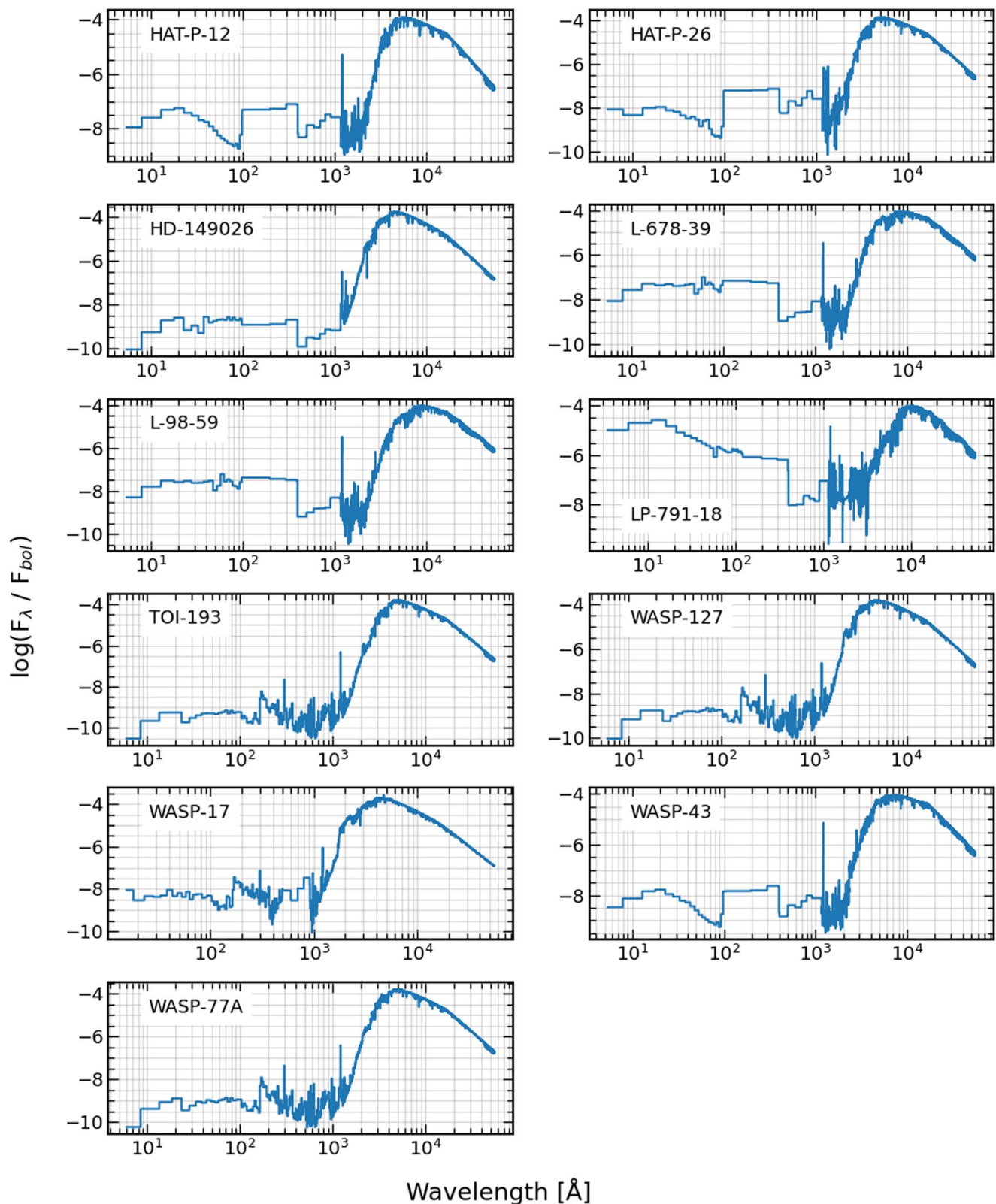
### 3.4. UV Irradiation Environment of Exoplanets

Here we present our FUV and NUV flux measurements in context of the closest orbiting planet for each system. Figure 8 shows the incident top-of-the-atmosphere FUV and NUV flux relative to the Earth/Sun system for the MUSCLES Extension targets and a subset of the original MUSCLES targets as well as flux incident at each stellar system’s conservative habitable zone, calculated as the average of the inner and outer habitable zone using the models of Kopparapu et al. (2013). Stars with a solar-like FUV/NUV ratio are those with little separation on the plot, while those with FUV/NUV ratios much different than the Sun (e.g., M dwarfs) have a large separation between FUV and NUV.

Many previous studies have used M dwarfs observed by the MUSCLES program as inputs to atmospheric models of hypothetical planets (e.g., Tian et al. 2014; Rugheimer et al. 2015; Chen et al. 2021). The MUSCLES Extension is the first time that FUV and NUV fluxes have been directly measured for an ensemble of stars whose planets have been or will be characterized with high-sensitivity spectrophotometric observations, allowing for more accurate modeling of photochemical contributions to atmospheric composition and evolution.

Planets around our G and F stars experience flux enhancements of  $\sim 10^3$ – $10^4$  relative to Earth/Sun in both the FUV and

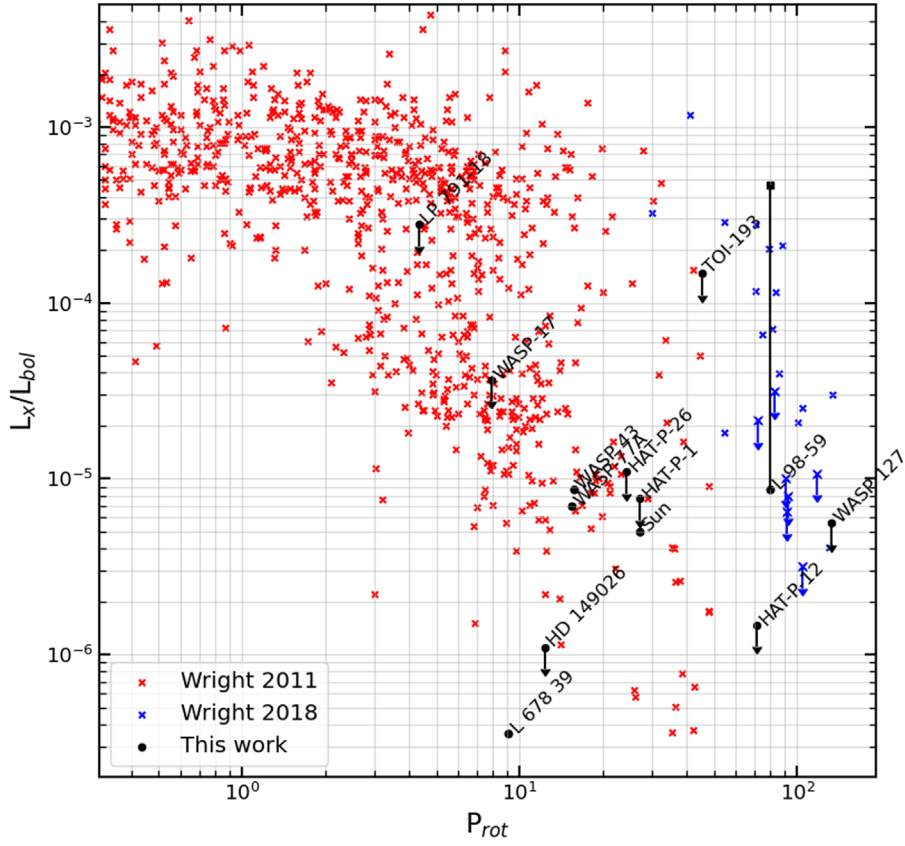




**Figure 3.** Panchromatic stellar SEDs from  $5 \text{ \AA}$ – $5.5 \text{ \mu m}$ . The vertical axis represents the flux density normalized by the bolometric flux, spanning approximately  $10^{-10}$ – $10^{-4} \text{ \AA}^{-1}$ . All spectra have been binned to  $5 \text{ \AA}$  per pixel for visualization.

NUV, due to their smaller semimajor axes. Notably, the smaller M and K stars show FUV enhancements of  $\sim 1$ – $2$  orders of magnitude more than that of the Earth/Sun but NUV decrements of  $\sim 1$  order of magnitude *less* than the Earth/

Sun system. This indicates a strong possibility of photochemical disequilibrium, as photodissociation rates in the FUV will be enhanced while those in the NUV, including  $\text{O}_3$ , will be suppressed relative to Earth.



**Figure 4.** Fraction of bolometric luminosity emitted in the X-ray. Wright et al. (2011) represents solar and late-type stars. Wright et al. (2018) represents fully convective M dwarfs. The black square connected by the vertical line to L 98-59 represents the X-ray luminosity during only the flaring event. The black circle representing L 98-59 shows the quiescent X-ray luminosity.

**Table 2**  
XMM-Newton Observations

Star	ObsID	Exp Time (ks)	Net Counts	Count Rate (s <sup>-1</sup> ) <sup>a</sup>	$F_x$ (erg s <sup>-1</sup> cm <sup>-2</sup> )	$L_x$ (erg s <sup>-1</sup> )	$L_x/L_{bol}$	Reference
HAT-P-12	0853380901	2.7875	1	<3.23 × 10 <sup>-3</sup>	<3.59 × 10 <sup>-15</sup>	<8.79 × 10 <sup>27</sup>	<1.10 × 10 <sup>-5</sup>	1
HAT-P-26	0804790101	14.041	7	<6.41 × 10 <sup>-4</sup>	<7.62 × 10 <sup>-16</sup>	<1.84 × 10 <sup>27</sup>	<1.10 × 10 <sup>-6</sup>	2
HD 149026	0763460301	15.55	62	2.32 ± 0.51 × 10 <sup>-3</sup>	5.19 ± 1.14 × 10 <sup>-15</sup>	3.59 ± 0.79 × 10 <sup>27</sup>	3.56 ± 0.78 × 10 <sup>-7</sup>	3
L 678-39	0840841501	22.409	69	2.67 ± 0.43 × 10 <sup>-3</sup>	2.73 ± 0.44 × 10 <sup>-15</sup>	2.65 ± 0.43 × 10 <sup>25</sup>	3.99 ± 0.64 × 10 <sup>-7</sup>	4
WASP-43	0871800101	21.21	81	3.39 ± 0.43 × 10 <sup>-3</sup>	3.56 ± 0.45 × 10 <sup>-15</sup>	3.22 ± 0.40 × 10 <sup>27</sup>	5.62 ± 0.70 × 10 <sup>-6</sup>	5
WASP-127	0853380601	1.0274	0	<8.76 × 10 <sup>-3</sup>	<1.26 × 10 <sup>-14</sup>	<3.86 × 10 <sup>28</sup>	<5.02 × 10 <sup>-6</sup>	1
L 98-59	0871800201	2.896	36	1.00 ± 0.20 × 10 <sup>-2</sup>	3.20 ± 0.06 × 10 <sup>-14</sup>	3.98 ± 0.73 × 10 <sup>26</sup>	8.72 ± 0.17 × 10 <sup>-6</sup>	5
L 98-59	0871800301	2.896	49	1.20 ± 0.20 × 10 <sup>-2</sup>	3.50 ± 0.05 × 10 <sup>-14</sup>	3.98 ± 0.55 × 10 <sup>26</sup>	9.43 ± 0.13 × 10 <sup>-6</sup>	5

**Note.**

<sup>a</sup> Upper limits represent the count rate required to produce a 3σ detection given the listed exposure time.

**References.** (1) XMM-Newton Target of Opportunity (proposal ID 085338; PI Shartel), (2) Sanz-Forcada (2016), (3) Salz (2014), (4) Stelzer (2020), (5) France et al. (2020a).

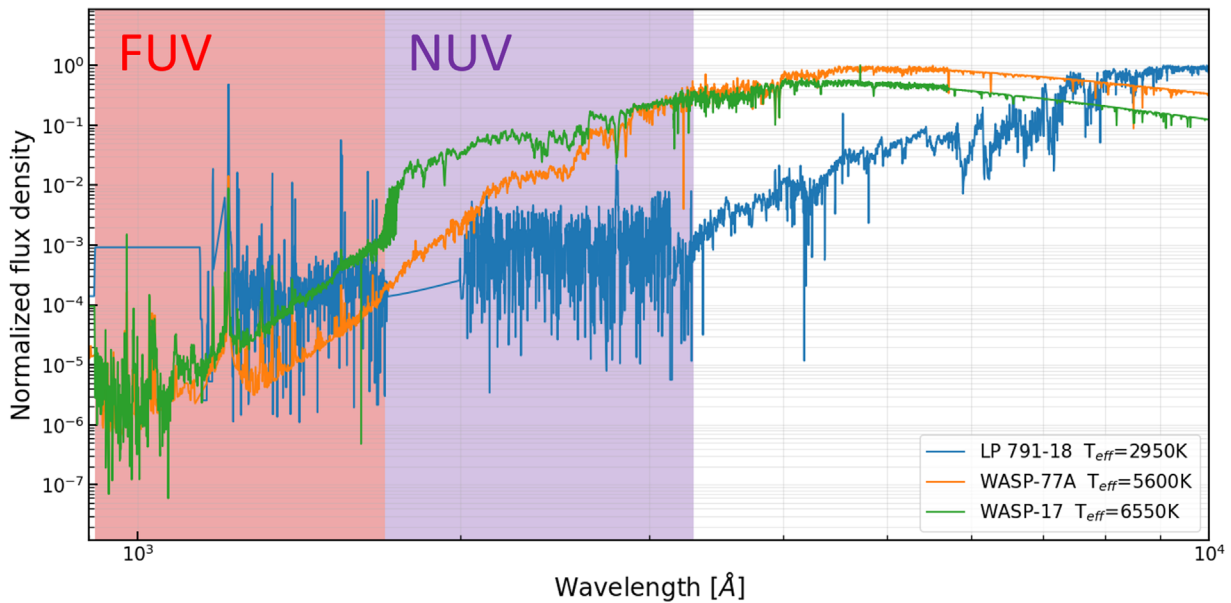
**Table 3**  
Chandra Observations

Star	ObsID	Exp Time (ks)	Net Counts	Count Rate (s <sup>-1</sup> ) <sup>a</sup>	$F_x$ (erg s <sup>-1</sup> cm <sup>-2</sup> )	$L_x$ (erg s <sup>-1</sup> )	$L_x/L_{bol}$	Reference
WASP-77A	15709	9.939	24	2.08 ± 0.05 × 10 <sup>-3</sup>	1.49 ± 0.33 × 10 <sup>-14</sup>	1.97 ± 0.44 × 10 <sup>28</sup>	6.97 ± 1.55 × 10 <sup>-6</sup>	1
WASP-17	23322	23.84	4	<3.78 × 10 <sup>-4</sup>	<2.85 × 10 <sup>-14</sup>	<5.73 × 10 <sup>29</sup>	<3.65 × 10 <sup>-5</sup>	2
LP 791-18	23320	23.79	2	<3.78 × 10 <sup>-4</sup>	<2.63 × 10 <sup>-14</sup>	<2.13 × 10 <sup>27</sup>	<2.79 × 10 <sup>-4</sup>	2
TOI-193	23321	22.89	1	<3.92 × 10 <sup>-4</sup>	<2.60 × 10 <sup>-14</sup>	<1.99 × 10 <sup>28</sup>	<7.68 × 10 <sup>-6</sup>	2

**Note.**

<sup>a</sup> Upper limits represent the count rate required to produce a 3σ detection given the listed exposure time.

**References.** (1) Salz (2013), (2) France et al. (2020a).



**Figure 5.** Stellar UV flux with increasing effective temperature. Note that increasing effective temperature drives the photospheric emission deeper into the UV, as discussed in Section 3.2

### 3.5. L 98-59 X-Ray Flare

We obtained two XMM-Newton observations of L 98-59, which each had an X-ray flaring event. The first was on 2021 April 15, 08:26:45 UTC (obs.ID 0871800201, hereafter F201) and the second on 2021 April 16, 03:27:28 UTC (obs.ID 0871800301, hereafter F301). Both flares were detected in the EPIC pn and MOS detectors (X-ray;  $\sim 0.3$ – $10.0$  keV), and F301 was also detected in the Optical Monitor with the UVW1 filter (OM UVW1; 2000–4000 Å). We extracted the light curves using the SAS *evselect* routine with a temporal bin size of 100 s. The two flares are shown together, relative to the beginning of their respective observations, in Figure 9. Defining the start time as the point where the light curve first exceeds the quiescent level, and the rise time as the difference between the time of peak count rate and the start time, we find that F301 had a start time of  $3300 \pm 50$  s and a rise time of  $400 \pm 70$  s. F201 had a start time of  $2900 \pm 50$  s and a longer rise time of  $1000 \pm 70$  s.

L 98-59 does not return to its quiescent level during the length of the observation for either flare; thus, we are unable to quantify a definitive duration. We report instead a lower limit duration, which is the time from flare start to the end of the usable observation. The flare durations are  $>15.7$  ks for F301 and  $>16.8$  ks for F201.

#### 3.5.1. Flare Luminosity and Equivalent Duration

The X-ray flare of L 98-59 produced enough counts to allow for spectral fitting. We use the XSPEC software (Arnaud 1996) with an VAPEC plasma model to model the stellar spectrum. Due to the time-variable plasma properties during a flaring event, spectral analysis of the flares was conducted by splitting each flare into four time intervals—quiescent, peak, decay, and tail regions. “Quiescent” is the pre-flare region, “peak” is the region of  $\sim 3$  ks centered on the peak of the flare, “decay” is the region of declining count rate until the rate begins to reach a constant value at  $\sim 10$  ks, and “tail” is the remainder of the exposure. We use a single- or double-temperature VAPEC

model to derive a characteristic plasma temperature for each time interval with metal abundances as described in the study of the M dwarf system LTT 1445 by Brown et al. (2022). The interstellar hydrogen column density was fixed at  $1 \times 10^{18}$   $\text{cm}^{-2}$ . The resulting flux from the best-fit VAPEC models was used to calculate the luminosities of each flare as

$$L_x = 4\pi d^2 \int F dE \quad (4)$$

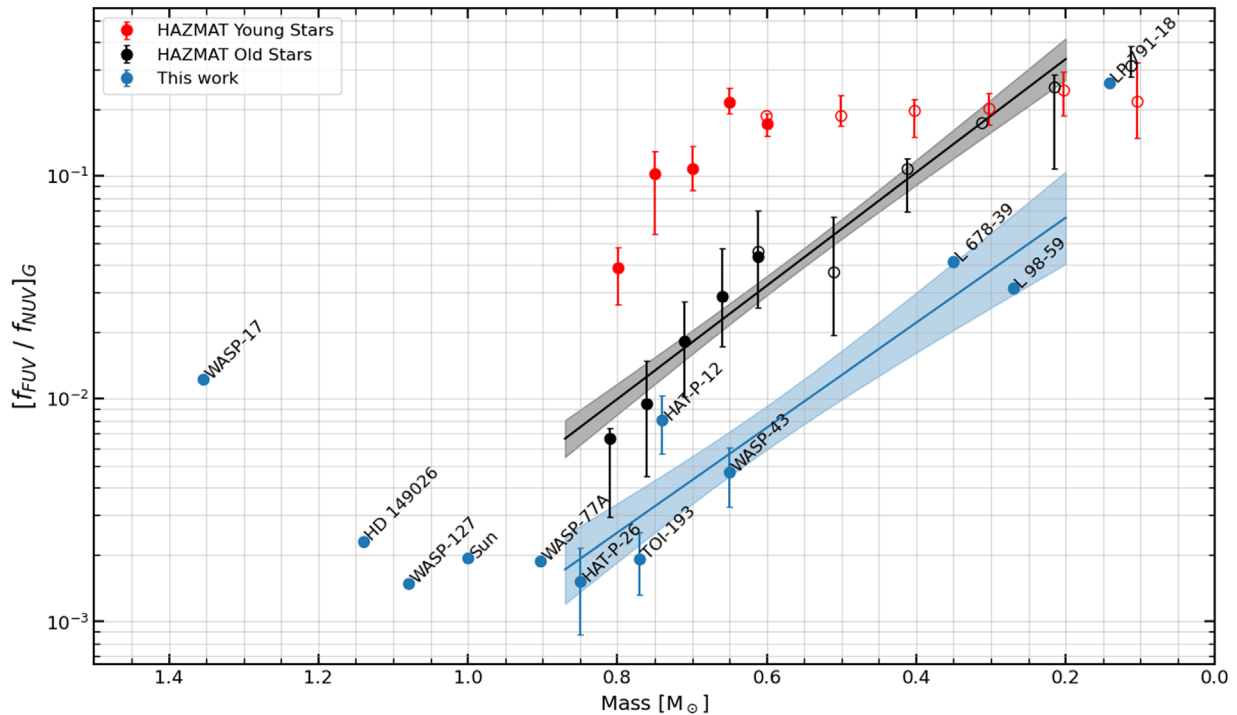
where  $0.3 < E < 10.0$  keV,  $d$  is the stellar distance, and  $F$  is the flux from the best-fit VAPEC models. The quiescent luminosities from the best-fit VAPEC models were  $L_x = 3.82 \pm 0.70 \times 10^{26}$   $\text{erg s}^{-1}$  and  $L_x = 4.13 \pm 0.57 \times 10^{26}$   $\text{erg s}^{-1}$  for F201 and F301, respectively. The calculated flare luminosities were  $L_x = 2.05 \pm 0.05 \times 10^{28}$   $\text{erg s}^{-1}$  for F201 and  $L_x = 1.59 \pm 0.40 \times 10^{28}$   $\text{erg s}^{-1}$  for F301. In comparison, a recent study of Proxima Centauri by Fuhrmeister et al. (2022) found that during an average flare the ratio of peak count rate to quiescent count rate is 10, and the average flare luminosity is  $L_x = 6.7 \times 10^{27}$   $\text{erg s}^{-1}$ . The VAPEC parameters and X-ray properties of both observations are listed in Table 5.

We also compute the equivalent duration,  $\delta$ , of each flare. The equivalent duration represents the amount of time it would take the star, in the quiescent state, to release the same amount of energy as is released during the flare (Gershberg 1972; Hunt-Walker et al. 2012):

$$\delta = \int_{t_0}^{t_0 + \Delta t} \frac{(R_f - R_q)}{R_q} dt \quad (5)$$

where  $t_0$  is the start time of the flare,  $\Delta t$  is the flare duration,  $R_f$  is the 0.3–10 keV count rate during the flare, and  $R_q$  is the 0.3–10 keV count rate during the quiescent period. The equivalent durations of the L 98-59 flares were  $\delta > 130.4$  ks for F301 and  $\delta > 245.9$  ks for F201. These are larger than the equivalent durations reported in Loyd et al. (2018), which had values  $1.3 < \delta < 120.9$  ks for similarly inactive M and K stars.





**Figure 6.** MUSCLES Extension stars are compared with M and K dwarfs from the HAZMAT surveys. For stars from the HAZMAT surveys, open markers indicate M dwarfs from Schneider & Shkolnik (2018) while solid markers represent K dwarfs from Richey-Yowell et al. (2019). Shaded regions represent the  $1\sigma$  error level of the linear fits.

However, two of three flares from the MUSCLES study were also truncated before the end of the flare duration and thus are also considered to be lower limits.

Accounting for the flares increases  $L_x/L_{\text{bol}}$  to  $38.5\times$  and  $53.7\times$  the quiescent level. This highlights the importance of accounting for high-energy flaring events in the XUV radiation environment of exoplanets around M dwarfs, especially as we have observed two similar events within a 24 hr period.

### 3.5.2. NUV Flare of F301

The OM UVW1 flare from F301 peaks during the rise time of the X-ray flare, shown in Figure 10. Güdel et al. (2002) reported a similar phenomenon during a flaring event of Proxima Centauri, for which they also obtained simultaneous XMM-Newton EPIC and OM UVW1 observations. Güdel et al. (2002) proposed a chromospheric evaporation scenario similar to the well-studied Neupert effect (Neupert 1968) in which a flaring event accelerates high-energy electrons into the chromosphere, where the subsequent deposition of energy causes a sharp optical signal and increase in chromospheric temperature driving hot plasma into the corona and resulting in the longer-duration X-ray flare. The Neupert effect was first described in relation to simultaneous hard X-ray and microwave flares in the solar corona but had not been seen in the X-ray and NUV/optical prior to its observations on other stars. The X-ray/optical relation has since been observed in several stellar spectra of M and K dwarfs: in BY Draconis (K4; de Jager et al. 1986), UV Ceti (M6; de Jager et al. 1986; Schmitt et al. 1993), AD Leonis (M3; Hawley et al. 1995), Proxima Centauri (M5.5; Güdel et al. 2002, 2004), and now L 98-59 (an “optically inactive” M3). If the chromospheric evaporation scenario proposed by Güdel et al. (2002) is correct, one should

expect the time derivative of the X-ray light curve to mimic the optical signal:

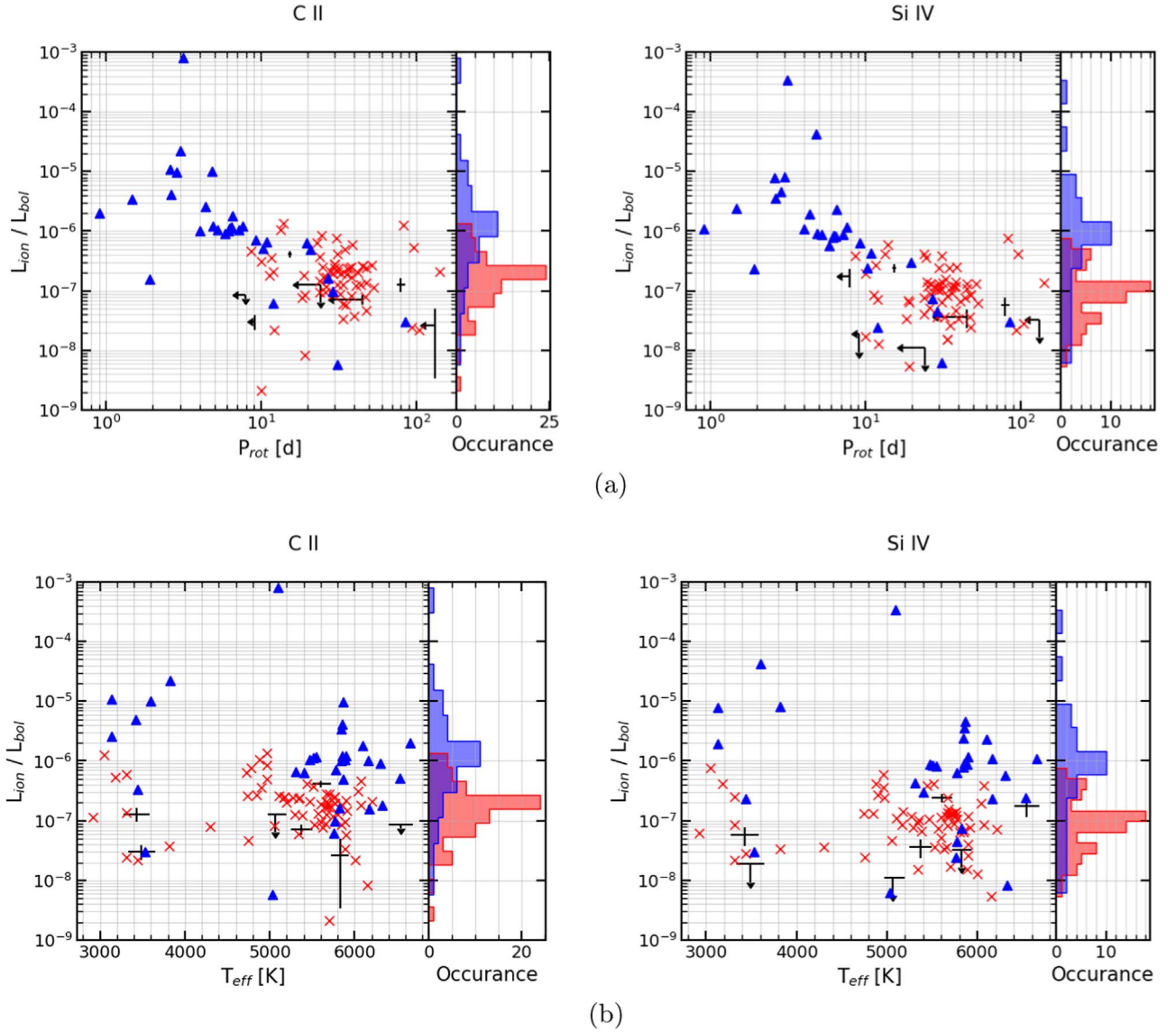
$$\frac{dL_x}{dt} \propto L_o. \quad (6)$$

Figure 10 shows light curves from the EPIC and OM UVW1 instruments during the F301 flaring event. We are not concerned with total counts in this analysis, and as such we have rebinned both X-ray and NUV light curves to 10 s intervals rather than 100 s to obtain more accurate temporal measurements. As expected from Equation (6), the time derivative of the X-ray light curve matches the shape of the OM UVW1 light curve (Figure 10(b)), with a difference in peak timing of  $27 \pm 7$  s. This supports the theory of chromospheric evaporation occurring during stellar flaring events.

## 4. Summary

The MUSCLES Extension for Atmospheric Transmission Spectroscopy is a study of UV and X-ray activity of 11 exoplanet-hosting stars whose systems are to be observed as part of the JWST ERS and GTO programs but that have no previous UV characterization. We obtained FUV and NUV observations of each target using HST-STIS and -COS, as well as a combination of new and archival X-ray observations using XMM-Newton and Chandra observatories. We assessed the chromospheric and transition-region activity levels of each star based on their FUV/NUV flux ratios and fraction of bolometric flux from X-rays and UV ion emission lines and put these activity measurements into context by comparing the MUSCLES extension targets to a broader population of planet- and non-planet-hosting stars.

The main results of this work are as follows:



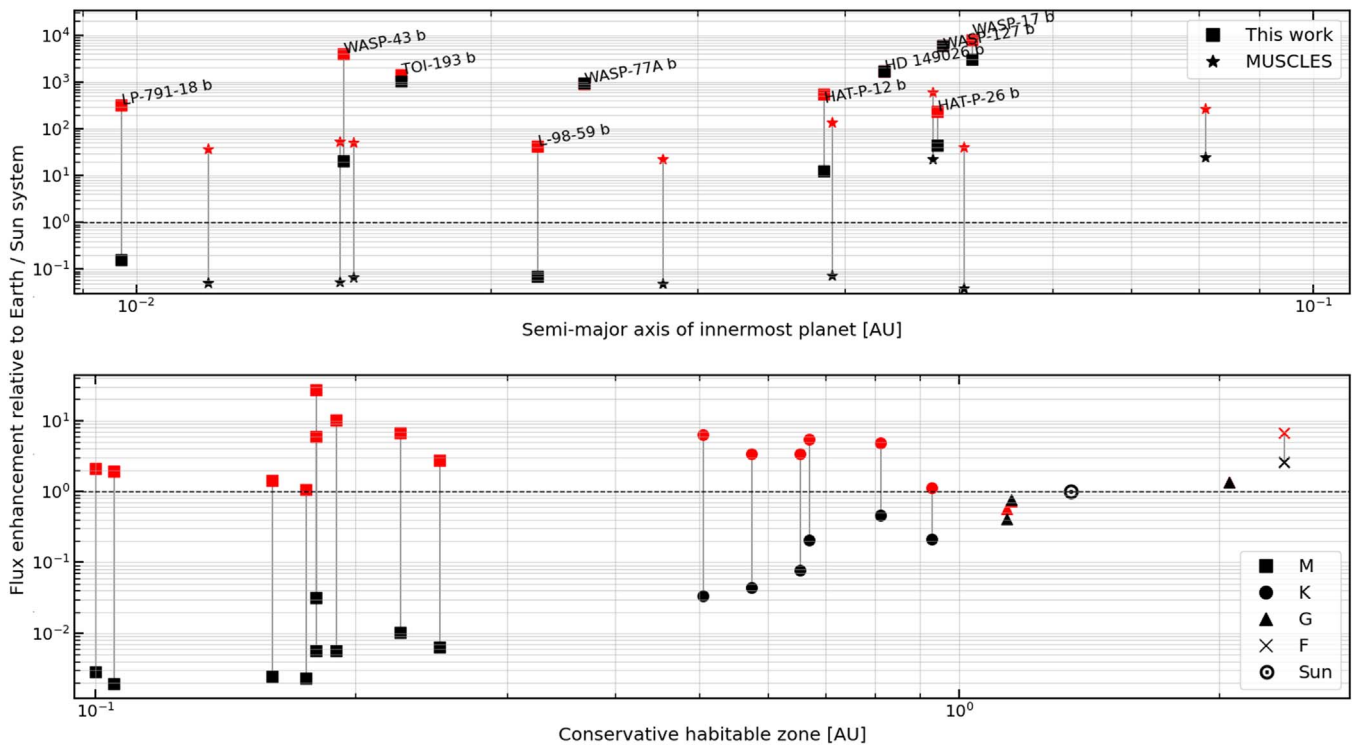
**Figure 7.** Fraction of bolometric luminosity of UV ions vs. (a) rotation period (b) effective temperature.  $\times$  = France et al. (2018) planet hosts,  $\blacktriangle$  = France et al. (2018) non-planet hosts, and  $+$  = this work. Histograms represent the number of stars with a bolometric luminosity ratio within the range of each bin, with blue corresponding to non-planet hosts and red to planet hosts.

**Table 4**  
Mean and Standard Deviations of C II and Si IV Fraction of Bolometric Luminosity

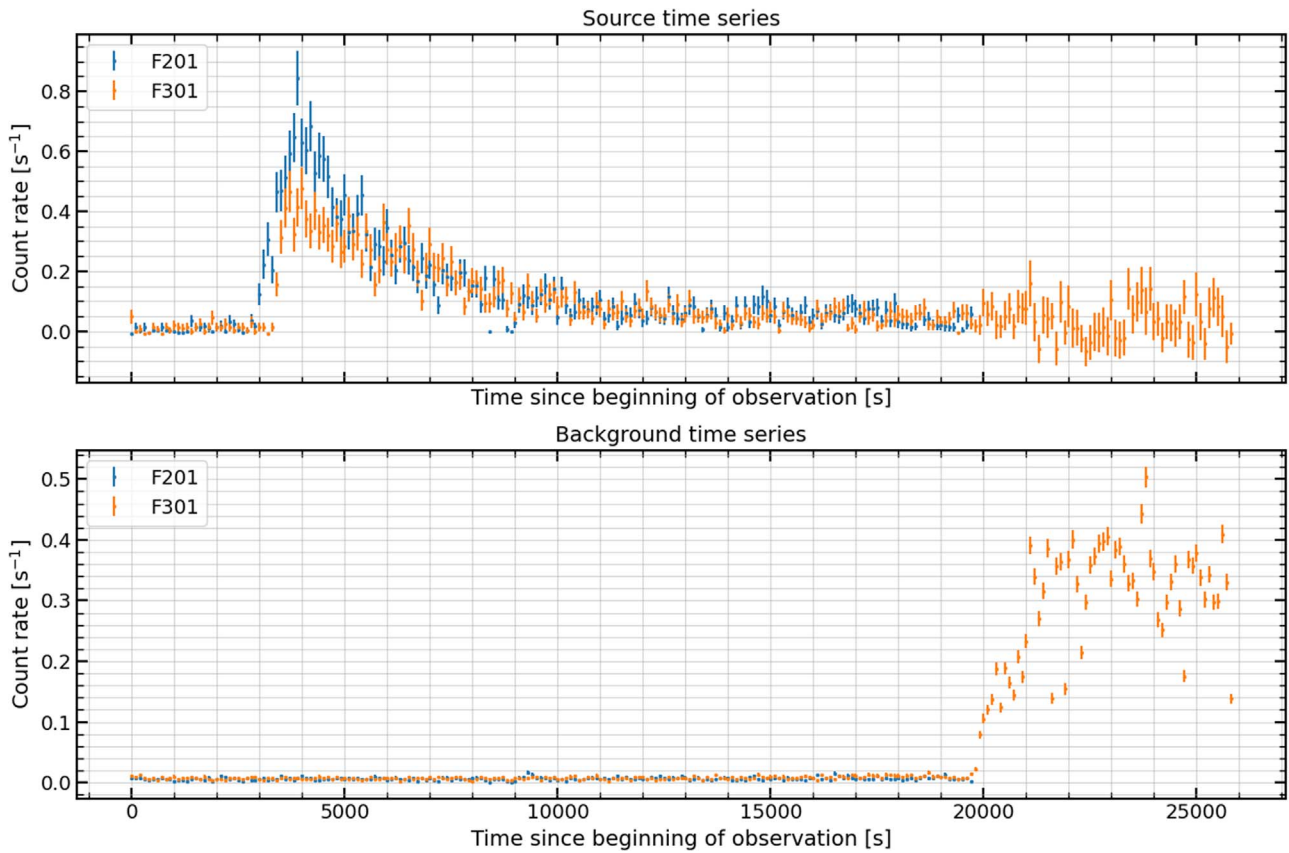
Stellar Population	C II Mean	C II Standard Deviation	Si IV Mean	Si IV Standard Deviation
Non-planet hosts	$2.75 \times 10^{-5}$	$1.40 \times 10^{-4}$	$1.39 \times 10^{-5}$	$6.09 \times 10^{-5}$
Planet hosts	$2.47 \times 10^{-7}$	$2.64 \times 10^{-7}$	$1.34 \times 10^{-7}$	$1.40 \times 10^{-7}$

1. We have assembled panchromatic SEDs from  $5.5 \text{ \AA} - 5 \mu\text{m}$  of 11 exoplanet-hosting stars with guaranteed JWST observation time but no prior UV characterization with HST. The SEDs will be available as high-level science products on the MUSCLES portal hosted on the MAST archive at doi:10.17909/T9DG6F and can be used as inputs for the stellar irradiance when modeling planetary atmospheres observed by JWST, eliminating the need to rely on optical scaling relations or stellar models without a complete treatment of the upper stellar atmospheres.
2. The planet-hosting stars from our survey follow the trend of France et al. (2018), displaying statistically lower

activity levels than non-planet-hosting groups on the basis of fractional X-ray luminosity, UV ion emission, and FUV/NUV flux ratios. This can easily be explained by a sample bias: confirmed exoplanets from RV and transit surveys largely select for low-activity stars, as active stars add excess noise to RV and transit measurements. However, as planet population estimates expect to find exoplanets around the vast majority of stars, selecting stellar irradiance levels based on samples of known exoplanet-host stars likely underestimates the UV flux experienced over a planet’s lifetime and is not indicative of the radiation environments of the exoplanet

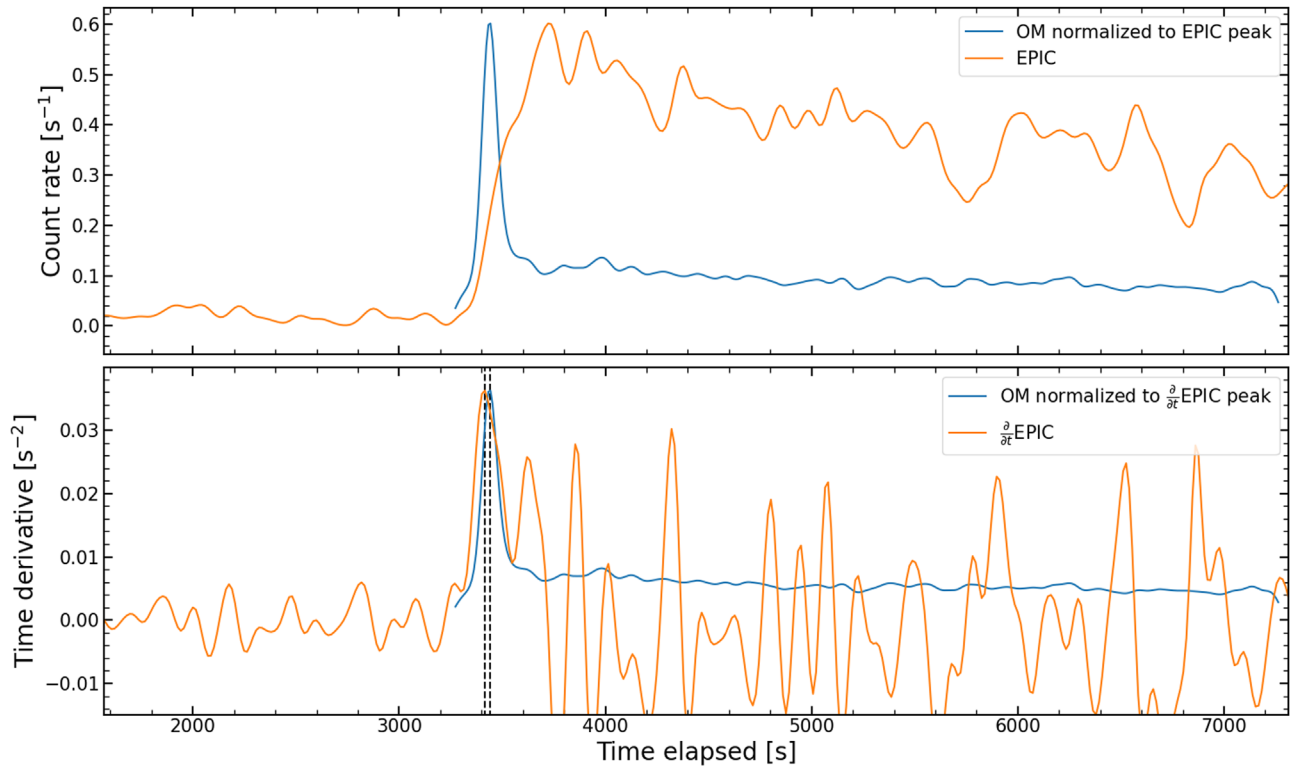


**Figure 8.** Top: UV flux incident at the top of the innermost planet’s atmosphere relative to the UV flux incident at Earth. Bottom: amount of flux incident at the conservative habitable zone (average of the inner- and outermost habitable zones using Kopparapu et al. 2013 models) relative to the flux experienced at the Sun’s habitable zone of approximately 1.3 au. For both panels, red markers indicate flux over the FUV band, and black markers indicate the NUV band.



**Figure 9.** Top: background-subtracted source light curves for F201 and F301. Bottom: background time series for each observation. Note the large background flare occurring at 20 ks in F301; this is likely due to protons within the Earth’s magnetosphere being funneled toward the detector. All data are from the EPIC pn detector with the medium filter and binned to 100 s.





**Figure 10.** L 98-59 X-ray and NUV light curves for F301. The EPIC light curves have been binned to 10 s to match the time resolution of the OM UVW1 data. The data have been smoothed with a Gaussian kernel for clarity. Top: OM UVW1 flare normalized to the peak of the X-ray flare. Bottom: time derivative of the X-ray flare (units of  $\text{s}^{-2}$ ) overplotted by the normalized OM UVW1 light curve (units of  $\text{s}^{-1}$ ). Note that the blue OM UVW1 curve does not match the units of the vertical axis and is only plotted here as a visual aid. The vertical black lines represent the location of the peak of each light curve.

**Table 5**  
Properties of L 98-59 X-Ray Flares

	0871800201 (F201)—Flare	0871800301 (F301)—Flare	F201—Quiescent	F301—Quiescent
Exposure time (ks)	14.039	13.819	2.896	2.896
Net counts	2298	1838	36	49
Count rate ( $\text{cnt s}^{-1}$ ) <sup>a</sup>	$0.502 \pm 0.002$	$0.295 \pm 0.001$	$0.010 \pm 0.002$	$0.012 \pm 0.002$
$f_x$ ( $10^{-13} \text{ erg s}^{-1} \text{ cm}^{-2}$ )	$17.1 \pm 0.4$	$13.2 \pm 0.3$	$0.32 \pm 0.06$	$0.35 \pm 0.05$
$\log L_x$ ( $\text{erg s}^{-1}$ )	$28.3 \pm 0.01$	$28.2 \pm 0.01$	$26.6 \pm 0.08$	$26.6 \pm 0.06$
$L_x/L_{\text{bol}}$	$4.68 \pm 0.02 \times 10^{-4}$	$3.63 \pm 0.02 \times 10^{-4}$	$8.72 \pm 0.17 \times 10^{-6}$	$9.43 \pm 0.13 \times 10^{-6}$
$L_x$ enhancement <sup>a</sup>	53.7	38.5	...	...
$kT_1$ (keV) <sup>b</sup>	$1.21^{+0.157}_{-0.169}$	$1.32^{+0.169}_{-0.189}$	...	...
$kT_2$ (keV) <sup>b</sup>	$0.268^{+0.095}_{-0.047}$	$0.294^{+0.128}_{-0.055}$	...	...
[Fe/H] <sup>b</sup>	$0.215^{+0.147}_{-0.167}$	$0.302^{+0.347}_{-0.202}$	...	...

**Notes.**

<sup>a</sup> Enhancement represents the ratio of X-ray luminosity during the peak region to the quiescent luminosity.

<sup>b</sup> Reported value is during the flare peak.

population at large. Therefore, we present a cautionary speculation that the UV-driven atmospheric photochemistry on the average galactic exoplanet may be significantly different than what we measure on the current set of planets being studied by JWST.

3. We find two X-ray flares on the M dwarf L 98-59 that increased the X-ray fraction of its bolometric luminosity by factors of 38.5 and 53.7 times the quiescent levels. Depending on the frequency of flaring events, this could significantly increase the total amount of XUV irradiation

of the planets orbiting this otherwise inactive star. This highlights the importance of studying time variability in exoplanet-hosting stars in order to accurately model a planet's lifetime-integrated UV irradiance.

**Acknowledgments**

The HST observations presented here were acquired as part of the Cycle 28 program 16166, supported by NASA through a grant from the Space Telescope Science Institute, which is

operated by the Association of Universities for Research in Astronomy, Inc., under NASA contract NAS 526555. This work is based in part on observations made by the Chandra X-ray Observatory, supported by Chandra grant G01-22022X to the University of Colorado, and by data obtained from the Chandra Data Archive, and based on observations obtained with XMM-Newton, an ESA science mission with instruments and contributions directly funded by ESA Member States and NASA.

This research has made use of the NASA Exoplanet Archive, which is operated by the California Institute of Technology, under contract with the National Aeronautics and Space Administration under the Exoplanet Exploration Program.

*Facilities:* HST, XMM-Newton, Chandra.

*Software:* astropy (Astropy Collaboration et al. 2013, 2018), scipy (Virtanen et al. 2020), matplotlib (Hunter 2007), SAO-Image DS9 (Smithsonian Astrophysical Observatory 2000), Scientific Analysis System (Gabriel et al. 2004), CIAO (Fruscione et al. 2006), XSPEC (Arnaud 1996).

## Appendix A Targets

The targets for the MUSCLES Extension include 3 M, 3 K, 5 G, and 1 F type dwarf stars. Notable differences from the original MUSCLES and Mega-MUSCLES survey are the inclusion of G and F type stars and the much larger distances to the targets. Our targets host a wide variety of exoplanets, from sub-Earth size through giant hot-Jupiters. This section is dedicated to providing a brief description of each planetary system as well as the spectral data used during construction of the SEDs.

### A.1. WASP-17

WASP-17 is an F6 star at a distance of approximately 405 pc based on Gaia Data Release 3 (DR3; Gaia Collaboration et al. 2022) data. The star is estimated to have a rotation period of 8.5–11 days and an age of approximately 2.7 Gyr with a subsolar metallicity of  $[\text{Fe}/\text{H}] = -0.190 \pm 0.090$  (Bonomo et al. 2017). The system consists of one confirmed and peculiar exoplanet. WASP-17b is an ultra-low-density planet with a radius of  $R_p \approx 2R_J$  but a mass of only  $M_p \approx 0.5M_J$ . Initial observations of WASP-17b (Anderson et al. 2010) suggested the planet has a retrograde orbit; this was later confirmed by Bayliss et al. (2010). The proposed explanation for WASP-17b’s retrograde orbit is a combination of planet–planet scattering, the Kozai mechanism, and tidal circularization (Anderson et al. 2010, and references therein).

We obtained STIS G140L, G230L, and G430L observations of WASP-17. The G140L spectra showed no evidence of FUV emission line flux and had poor quality over the Ly $\alpha$  region. We did not obtain G140M spectra, and therefore were unable to reconstruct the Ly $\alpha$  emission line using MCMC methods, but the strong S/N in the NUV G230L observations allowed for estimation using the Mg II relation.

We obtain 23.84 ks of new Chandra ACIS-S observations (obs.ID 201354, PI France) of WASP-17. Our X-ray analysis of the target was a nondetection, and we present a  $3\sigma$  upper limit for our further X-ray analysis as discussed in Section 2.2.

The proxy star used for the X-ray and FUV spectrum was Procyon, an F5 star with  $T_{\text{eff}} \approx 7740$  K. We obtained a high-resolution UV spectrum of Procyon from the SISTINE II

sounding rocket observation (Cruz-Aguirre et al. 2023, in preparation). The effective temperature of Procyon is  $\sim 1200$  K higher than WASP-17, but we find that the NUV scaling procedure matched the shape of the spectrum very well in the G230L region from 1750–3150 Å, and we find that Procyon has  $L_x/L_{\text{bol}} \sim 1 \times 10^{-5}$ , similar to the upper limit of WASP-17. Thus, we believe that Procyon is a suitable proxy star for WASP-17.

### A.2. HD 149026

HD-149026 is a G0 star with a DR3 distance of approximately 76 pc. The star has a supersolar metallicity,  $[\text{Fe}/\text{H}] = 0.36 \pm 0.05$ , and a single confirmed exoplanet with an unusually dense core (Sato et al. 2005). The exoplanet, HD 149026b, has a radius of  $R = 0.725 \pm 0.05 R_J$  but a density of 1.7 times that of Saturn. The high metallicity of the system in conjunction with the high density of the planet indicate that it may have an icy/rocky core that makes up 50%–80% of the planetary mass (Sato et al. 2005; Fortney et al. 2006).

We obtained STIS G140L, G140M, E230M, and G430L observations of HD-149026. During the G140L observations, the shutter door remained closed for the entire duration, and thus no spectra were acquired. Of the two G140M observations, the second had a misplaced extraction box during the X1DCORR routine and had to be re-extracted. After re-extraction we found the S/N of the G140M observations to be sufficient to reconstruct the Ly $\alpha$  emission line. The E230M spectrum has S/N above the threshold for all wavelengths and has been convolved to match the resolution of the G230L spectra used in the rest of the SEDs. The G430L observation has S/N above the threshold for all wavelengths  $\lambda \gtrsim 3050$  Å.

We retrieved 10.8 ks of archival XMM-Newton observations (obs.ID 0763460301, PI Salz) in which the target is detected, and we find an X-ray luminosity of  $\log L_x = 27.6 \pm 0.1 \times 10^{26}$  erg s $^{-1}$ .

Due to similar spectral type and rotation period, the proxy star for this target is the quiet Sun (Woods et al. 2009).

### A.3. WASP-127

WASP-127 is a G5 star with an estimated age of approximately 11 Gyr (Lam et al. 2017) and DR3 distance of 160 pc. Its planetary companion, WASP-127b, has an anomalously low density, with a sub-Saturn mass of  $M = 0.18 \pm 0.02 M_J$ , super-Jupiter radius of  $R = 1.37 \pm 0.04 R_J$ , and orbital period of 4.17 days; WASP-127b falls within the previously discussed sub-Neptune desert (Lam et al. 2017; Skaf et al. 2020). Transmission spectroscopy of WASP-127b shows a feature-rich spectrum including absorption by Na, H $_2$ O, and either CO $_2$  or CO (Spake et al. 2021). Additionally, the low-density “puffiness” of WASP-127b’s atmosphere is unlikely to be caused by photoevaporation due to its host star’s low UV flux (Palle et al. 2017; Skaf et al. 2020), making it an interesting target for alternative atmospheric inflation processes (see Skaf et al. 2020, and references therein).

We obtained STIS G140L, G140M, G230L, and G430L observations of WASP-127. The FUV G140L spectrum showed no evidence of FUV emission lines, and the Ly $\alpha$  emission from G140M was insufficient to recreate the intrinsic emission from MCMC methods so we opted to use the Mg II

scaling relation. The NUV G230L spectrum breaks the  $S/N > 3$  threshold for wavelengths of  $\lambda > 2050 \text{ \AA}$  and extremely faint Mg II emission.

We retrieved 8 ks of archival XMM-Newton observations (obs.ID 0853380601, PI Schartel), which yielded a nondetection of the target.

The X-ray and FUV proxy for WASP-127 is the quiet Sun. Despite its higher  $T_{\text{eff}}$ , we chose the solar spectrum based on its similarly low chromospheric and coronal activity levels and found that it provides a good fit to the stellar continuum below  $\sim 2600 \text{ \AA}$ .

#### A.4. TOI-193

TOI-193, also designated LTT 9779, is a solar-like G7 star with DR3 a distance of 81 pc. It has an estimated age of 2 Gyr and a supersolar metallicity of  $[\text{Fe}/\text{H}] = 0.25 \pm 0.04$  (Jenkins et al. 2020). Jenkins et al. (2020) confirmed an exoplanet, TOI-193b, with a mass of  $M = 9.225^{+0.25}_{-0.26} \times 10^{-2} M_J$ , radius of  $R = 0.421 \pm 0.02 R_J$ , and orbital period of 0.79d. Like WASP-127b, this places TOI-193b firmly within the Neptune desert, offering another opportunity to study the region between hot-Jupiters and super-Earths.

We obtained STIS G140L, G140M, G230L, and G430L observations of TOI-193. The G140L FUV observations did not show any emission lines above the  $S/N > 3$  threshold. We detect  $\text{Ly}\alpha$  emission in the G140M spectrum albeit with low  $S/N$ . Despite the quality, we were able to reconstruct the  $\text{Ly}\alpha$  emission line from G140M observations. The G230L NUV spectrum breaks the  $S/N$  threshold for wavelengths of  $\lambda > 2200 \text{ \AA}$  and shows faint Mg II emission within the photospheric absorption band.

We also obtained a new 22.89 ks Chandra ACIS-S observation of TOI-193, which showed a nondetection.

The X-ray and FUV proxy star chosen was again the quiet solar spectrum based on similar UV activity level indicators.

#### A.5. WASP-77A

WASP-77A is a G8 star with a K-dwarf companion. It has a DR3 distance of 105 pc. Maxted et al. (2013) reported WASP-77A to be solar-like in mass, radius, and metallicity; follow-up observations by Cortés-Zuleta et al. (2020) yield a slightly subsolar metallicity of  $[\text{Fe}/\text{H}] = -0.10^{+0.10}_{-0.11}$ . Maxted et al. (2013) reported an age of  $\sim 1$  Gyr using a rotation period relation or an age of  $\sim 8$  Gyr using stellar models. Following studies by Bonomo et al. (2017), Cortés-Zuleta et al. (2020) reported an age of  $\sim 6$  Gyr and a  $\log R'_{\text{HK}} = -4.57 \pm 0.02$  (Salz et al. 2015), indicating a low-activity, subsolar star. The single confirmed exoplanet, WASP-77Ab, is a typical hot-Jupiter with  $M = 1.76 \pm 0.06 M_J$ ,  $R = 1.21 \pm 0.02 R_J$ , and period of 1.36 days (Maxted et al. 2013). It is estimated to have a high mass-loss rate from previous X-ray studies (Salz et al. 2015) and provides a promising opportunity to study hot-Jupiter planets around solar-like stars.

We obtained STIS G140L, G140M, G230L, and G430L observations of WASP-77A. We find that the STIS FUV observations have  $S/N > 3$  for most emission lines. However, despite good  $S/N$  in the emission lines, we were unable to reconstruct the  $\text{Ly}\alpha$  line using the MCMC method and so report the estimated flux based on the Mg II relation. The G230L NUV observations break the  $S/N > 3$  threshold for

wavelengths of  $\lambda > 2000 \text{ \AA}$  and show Mg II in emission within the photospheric absorption band.

We retrieved 9.94 ks of archival Chandra ACIS-S observations (obs.ID 15709, PI Salz) in which the target is detected with a fractional X-ray luminosity of  $\log L_x/L_{\text{bol}} = -4.25$ .

The X-ray and FUV proxy star was again the quiet solar spectrum based on similar X-ray and UV activity level indicators.

#### A.6. HAT-P-26

HAT-P-26 is a K1 star with a DR3 distance of 142 pc. Initial observations (Hartman et al. 2011) reported the star to be slightly smaller than the Sun with a similar metallicity of  $[\text{Fe}/\text{H}] = -0.04 \pm 0.08$ . The system has an age of  $9.0^{+3.0}_{-4.9}$  Gyr and  $\log R'_{\text{HK}} = -4.992$  (Hartman et al. 2011); this indicates that HAT-P-26 is an old and inactive star. The exoplanet, HAT-P-26b, is a Neptune-sized planet with  $M = 0.059 \pm 0.007 M_J$ ,  $R = 0.565^{+0.072}_{-0.032} R_J$ , and period of 4.23 days (Hartman et al. 2011), making it the third star from this study that falls in the Neptune desert. It is notable for its low density, which is consistent with an irradiated planet with  $10 M_{\oplus}$  rocky core and  $8 M_{\oplus}$  gas envelope (Hartman et al. 2011; based on Fortney et al. 2007). Hartman et al. (2011) suggested that HAT-P-26b may have started its life as a Jupiter-sized planet and lost  $\sim 30\%$  of its initial mass based on the energy-limited escape described by Erkaev et al. (2007) and Yelle et al. (2008). However, Hartman et al. (2011) noted that due to the lack of knowledge of the XUV flux of its host star, the exact value of HAT-P-26b's mass loss is poorly constrained.

We obtained STIS observations with the G140L, G140M, G230L, and G430L gratings. Other than  $\text{Ly}\alpha$ , we find no UV emission lines with flux greater than the noise level in either the G140L or G140M observations. We also find no evidence of Mg II emission despite having good  $S/N$  beyond  $2550 \text{ \AA}$  in the G230L observation. This is consistent with Hartman et al.'s (2011) claim of HAT-P-26 being an inactive star. We were unable to reconstruct the  $\text{Ly}\alpha$  emission profile and instead report an upper-limit  $\text{Ly}\alpha$  flux based on the rms value of the continuum-subtracted region over the Mg II line, which we consider to be an upper limit of the Mg II flux.

We retrieved 17 ks of archival XMM-Newton observations (obs.ID 0804790101, PI Sanz-Forcada). Our analysis of the observation showed a nondetection.

The X-ray and FUV proxy for HAT-P-26 is HD 40307, a K2.5 dwarf observed during the MUSCLES survey.

#### A.7. HAT-P-12

HAT-P-12 is a K4 dwarf with a DR3 distance of 143 pc and a subsolar metallicity of  $[\text{Fe}/\text{H}] = -0.29 \pm 0.05$ . The single confirmed exoplanet, HAT-P-12b, first reported by Hartman et al. (2009), is a low-density gas giant with mass  $M_p = 0.211 \pm 0.012 M_J$  and radius  $R_p = 0.959^{+0.029}_{-0.021} R_J$ , with an orbital period of 3.21 days. HAT-P-12b is found to be consistent with models of an irradiated planet with a  $\lesssim 10 M_{\oplus}$  rocky core and an H/He dominated gas envelope (Hartman et al. 2009, and references therein).

Due to its large distance and expected low activity, G140L and G140M exposure times required to obtain  $S/N$  greater than the threshold were prohibitively long, and thus we obtained no G140L or G140M observations of HAT-P-12. Therefore, we cannot report any FUV emission line fluxes. However, we



obtained both G230L and G430L observations with good S/N for wavelengths  $\lambda > 2500 \text{ \AA}$  and were able to recreate the Ly $\alpha$  emission line based on the Mg II relation.

We retrieved 10 ks of archival XMM-Newton observations (obs.ID 0853380901, PI Schartel). Our analysis of the observation showed a nondetection.

The X-ray and FUV proxy for HAT-P-12 is HD 85512, a K6 dwarf observed in the MUSCLES survey.

#### A.8. WASP-43

WASP-43 is a K7 star with a DR3 distance of 87 pc. The exoplanet, WASP-43b, was first reported by Hellier et al. (2011) as a hot-Jupiter with mass and radius  $M_p = 2.0 \pm 0.1 M_J$  and  $R_p = 1.06 \pm 0.05 R_J$ , respectively, orbiting very close to the host star with a semimajor axis of 0.014 au and period of 0.813 days. Follow-up observations using TRAPPIST by Gillon et al. (2012) confirmed these parameters with higher precision. Based on stellar rotation period, WASP-43 is estimated to be a young star around 0.4 Gyr (Hellier et al. 2011); however, using the Fortney et al. (2010) relation between radius and age for a low-irradiation planet, Gillon et al. (2012) claimed that WASP-43b is consistent with a much older planet. This discrepancy is also noted by Husnoo et al. (2012) and may potentially be explained by tidal interactions between the large planet and low-mass star, leading to an increased stellar rotation rate and therefore an artificially younger age based on age–period relations (Pont 2009; Brown et al. 2011; Poppenhaeger & Wolk 2014). The results from our own stellar activity analysis show that WASP-43 is consistent with the population of old ( $\sim 5$  Gyr) inactive stars.

Due to large distance and expected low activity, we obtained no FUV observations of WASP-43 with the G140L or G140M gratings. We obtained NUV spectra with G230L and G430L with S/N above the threshold for wavelengths of  $\lambda > 2600 \text{ \AA}$ , including a strong Mg II emission line.

We obtained 28 ks of XMM-Newton observations (obs.ID 0871800101, PI France) of WASP-43. The target was detected on the EPIC pn detector and OM, and we find no evidence of flaring activity.

The X-ray and FUV proxy for WASP-43 is the K7 dwarf HD 85512.

#### A.9. L 678-39

L 678-39 (GJ 357, TOI-562) is a M2.5 dwarf with a DR3 distance of 9 pc and a subsolar to solar metallicity of  $[\text{Fe}/\text{H}] = -0.12 \pm 0.16$  (Schweitzer et al. 2019). A long stellar rotation period, low  $\log R'_{\text{HK}}$  value of  $-5.37$ , and low X-ray flux place the star in a regime of old age and low activity (Luque et al. 2019; Modirrousta-Galian et al. 2020). The L 678-39 system contains three confirmed exoplanets consisting of one Earth-sized planet and two super-Earth planets (Luque et al. 2019). The Earth-sized planet L 678-39b (GJ 357b) has a mass of  $M_p = 1.84 \pm 0.31 M_{\oplus}$  and radius  $R_p = 1.217^{+0.084}_{-0.083} R_{\oplus}$  and is the closest to the host star at a distance of  $a_p = 0.035 \pm 0.002$  au and an orbital period of 3.93 days. This system, along with the other two M dwarf systems in our study, is of interest due to the ongoing debate regarding the habitability of Earth-like planets around M dwarf stars.

We obtained FUV observations with the COS G130M and G160M gratings as well as STIS G140M for the Ly $\alpha$  emission.

The high spectral resolution of the COS gratings provided good S/N over the FUV emission regions, and we find a strong Ly $\alpha$  emission and reconstruct the intrinsic profile using the MCMC method of Section 2.4. The NUV spectrum was obtained with STIS G230L and G430L and breaches the S/N  $> 3$  threshold for wavelengths of  $\lambda > 2600 \text{ \AA}$ . We detect a significant Mg II emission in the G230L spectrum.

We obtained a 33 ks archival XMM-Newton observation (obs.ID 0840841501, PI Stelzer) in which L 678-39 was detected with the high-sensitivity EPIC pn detector. We find no evidence of flaring activity.

The X-ray and FUV proxy for L 678-39 is the M1.5 dwarf GJ 832.

#### A.10. L 98-59

L 98-59 (TOI-175) is a M3 dwarf with a DR3 distance of 10 pc and a metallicity of  $[\text{Fe}/\text{H}] = -0.5 \pm 0.5$  (Cloutier et al. 2019; Kostov et al. 2019). Cloutier et al. (2019) reported  $\log R'_{\text{HK}} = -5.4 \pm 0.11$ . Combined with a rotational period of  $p_{\text{rot}} \approx 78$  days, this indicates an old, low-activity star (Astudillo-Defru et al. 2017).

The system consists of four confirmed Earth- to sub-Neptune-sized planets (L 98-59b,c,d, Kostov et al. 2019; L 98-59d, Demangeon et al. 2021) and has gained much interest in the few years since its original discovery, prompting several follow-up studies and observation proposals (Cloutier et al. 2019; Barclay et al. 2021; Howard et al. 2021; Pidhorodetska et al. 2021). In this work we consider only L 98-59b. L 98-59b has a mass of  $M_p = 0.4^{+0.16}_{-0.15} M_{\oplus}$  (Demangeon et al. 2021), radius of  $R_p = 0.80 \pm 0.05 M_{\oplus}$ , and period of 2.25 days (Kostov et al. 2019).

We obtained observations of L 98-59 with the STIS G140L, G140M, G230L, and G430L gratings. We find FUV emission lines greater than the S/N  $> 3$  threshold in the G140L spectra and strong Ly $\alpha$  emission in the G140M observations. Thus, our FUV emission line fluxes are relatively well constrained, and we were able to reconstruct the Ly $\alpha$  line using the MCMC method. Our measurements of the FUV emission line fluxes and X-ray luminosity are consistent with the previous findings of low chromospheric activity. The G230L NUV observations break the S/N threshold for wavelengths of  $\lambda > 2600 \text{ \AA}$ .

We obtained two new XMM-Newton observations (obs.ID 0871800201 and 0871800301, PI France) of duration 23 ks and 29.1 ks, respectively. The target was detected in both the EPIC pn and MOS detectors as well as the OM. Despite the target's low activity level indicators mentioned above, we find flaring events in both EPIC and OM detections, which occur  $\sim 24$  hr apart. These flares are discussed in detail in Section 3.5.

The X-ray and FUV proxy star for L 98-59 is again GJ 832.

#### A.11. LP 791-18

LP 791-18 is an M6 dwarf with a DR3 distance of 26 pc and an approximately solar metallicity  $[\text{Fe}/\text{H}] = -0.09 \pm 0.19$ . Age estimates from  $v \sin i$  provide a lower limit of  $> 5$  Gyr (Crossfield et al. 2019). The star is host to two confirmed exoplanets: a super-Earth with  $R_p = 1.1 R_{\oplus}$  and a sub-Neptune with  $R_p = 2.3 R_{\oplus}$ . The planets have assumed but unconfirmed masses of  $2 M_{\oplus}$  and  $7 M_{\oplus}$ , respectively (Crossfield et al. 2019). We consider only the innermost planet, LP 791-18b. At the time of its discovery, this system was the third coolest

confirmed exoplanet-hosting star—second to Teegarden’s Star and TRAPPIST-1—making it of great interest to study the dynamics of multiplanet systems around small, very cool stars (Crossfield et al. 2019).

Due to the expected faintness of the target, we obtained only NUV observations with the STIS G230L and G430L gratings. The G230L spectrum never breaks the S/N >3 threshold except in the Mg II region, which shows a faint emission line. The G430L spectrum did not break the S/N threshold until wavelengths of  $\lambda > 3800 \text{ \AA}$ .

We obtained 23.79 ks of new Chandra observation of LP 791-18 with the ACIS-S instrument (obs.ID 23320, PI France). Our analysis of the observation showed a nondetection.

The X-ray and FUV proxy for LP 791-18 is Proxima Centauri (GJ 551), a  $\sim 5$  Gyr M5.5 dwarf.

## Appendix B UV Flux Measurements

Table 6 and Table 7 provide a list of UV ion emission line fluxes or upper limits measured from our HST observations.

**Table 6**  
UV Emission Line Flux Measurements [ $\text{erg s}^{-1} \text{ cm}^{-2}$ ]<sup>a</sup>

Star	$F_{\text{Si III}} \lambda 1206$	$F_{\text{N V}} \lambda \lambda 1239, 1243$	$F_{\text{C II}} \lambda 1335$
WASP-17	...	$< 1.02 \times 10^{-17}$	$< 3.64 \times 10^{-18}$
HD 149026	...	$6.84 \pm 0.59 \times 10^{-16}$	$3.64 \pm 0.13 \times 10^{-15}$
WASP-127	$< 3.68 \times 10^{-15}$	$< 2.66 \times 10^{-17}$	$< 2.84 \times 10^{-17}$
WASP-77A	$5.30 \pm 1.27 \times 10^{-16}$	$< 4.95 \times 10^{-17}$	$1.93 \pm 0.07 \times 10^{-15}$
TOI-193	$< 5.16 \times 10^{-15}$	$< 3.55 \times 10^{-17}$	$6.061 \pm 0.45 \times 10^{-16}$
HAT-P-26	$< 4.18 \times 10^{-15}$	$< 2.60 \times 10^{-17}$	$< 7.58 \times 10^{-17}$
HAT-P-12	...	...	...
WASP-43	...	...	...
L 678-39	$1.17 \pm 0.27 \times 10^{-16}$	$1.29 \pm 0.30 \times 10^{-16}$	$2.09 \pm 0.44 \times 10^{-16}$
L 98-59	$< 2.40 \times 10^{-15}$	$6.478 \pm 0.40 \times 10^{-16}$	$8.92 \pm 0.37 \times 10^{-16}$
LP 791-18	...	...	...

### Note.

<sup>a</sup> Upper-limit values represent nondetected emission lines. The upper-limit value reported is the rms of the continuum-subtracted line region. Entries with a solid horizontal line represent no available data.

**Table 7**  
UV Emission Line Flux Measurements Cont. [ $\text{erg s}^{-1} \text{ cm}^{-2}$ ]<sup>a</sup>






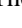





Star	$F_{\text{Si IV}} \lambda \lambda 1394, 1403$	$F_{\text{C IV}} \lambda \lambda 1548, 1551$	$F_{\text{Mg II}} \lambda \lambda 2799, 2803$	$F_{\text{Ly}\alpha}$ <sup>b</sup>
WASP-17	$< 1.31 \times 10^{-17}$	$< 1.58 \times 10^{-16}$	$7.50 \pm 0.50 \times 10^{-15}$	$2.85 \times 10^{-15}$
HD 149026	$1.92 \pm 0.11 \times 10^{-15}$	$3.52 \pm 0.23 \times 10^{-15}$	$1.65 \pm 0.08 \times 10^{-13}$	$2.01 \pm 0.37 \times 10^{-14}$
WASP-127	$< 3.20 \times 10^{-17}$	$< 1.73 \times 10^{-17}$	$1.59 \pm 0.20 \times 10^{-14}$	$4.96 \times 10^{-15}$
WASP-77A	$2.36 \pm 0.08 \times 10^{-15}$	$2.87 \pm 0.13 \times 10^{-15}$	$2.20 \pm 0.10 \times 10^{-14}$	$7.41 \times 10^{-15}$
TOI-193	$< 3.35 \times 10^{-17}$	$1.11 \pm 0.10 \times 10^{-15}$	$1.81 \pm 0.21 \times 10^{-14}$	$5.09 \times 10^{-15}$
HAT-P-26	$< 9.34 \times 10^{-18}$	$< 3.99 \times 10^{-17}$	$< 4.62 \times 10^{-16}$	$< 2.87 \times 10^{-15}$
HAT-P-12	...	...	$5.14 \pm 0.09 \times 10^{-15}$	$8.95 \pm 0.19 \times 10^{-15}$
WASP-43	...	...	$2.18 \pm 0.02 \times 10^{-14}$	$3.31 \times 10^{-14}$
L 678-39	$5.30 \pm 7.41 \times 10^{-17}$	$5.82 \pm 1.84 \times 10^{-16}$	$2.29 \pm 0.03 \times 10^{-14}$	$7.56 \pm 0.17 \times 10^{-14}$
L 98-59	$7.94 \pm 0.43 \times 10^{-16}$	$3.12 \pm 0.10 \times 10^{-15}$	$1.84 \pm 0.02 \times 10^{-14}$	$5.57 \pm 0.11 \times 10^{-14}$
LP 791-18	...	...	$1.72 \pm 0.07 \times 10^{-15}$	$7.59 \times 10^{-15}$

### Notes.

<sup>a</sup> Upper-limit values represent nondetected emission lines. The upper-limit value reported is the rms of the continuum-subtracted line region. Entries with a solid horizontal line represent no available data.

<sup>b</sup> Ly $\alpha$  was detected in HAT-P-26 but is reported as an upper limit because we were unable to reconstruct the line profile and relied on the upper limit of the Mg II flux value.

## ORCID iDs

Patrick R. Behr  <https://orcid.org/0000-0003-1369-8551>  
 Kevin France  <https://orcid.org/0000-0002-1002-3674>  
 Alexander Brown  <https://orcid.org/0000-0003-2631-3905>  
 Girish Duvvuri  <https://orcid.org/0000-0002-7119-2543>  
 Jacob L. Bean  <https://orcid.org/0000-0003-4733-6532>  
 Zachory Berta-Thompson  <https://orcid.org/0000-0002-3321-4924>  
 Cynthia Froning  <https://orcid.org/0000-0001-8499-2892>  
 Yamila Miguel  <https://orcid.org/0000-0002-0747-8862>  
 J. Sebastian Pineda  <https://orcid.org/0000-0002-4489-0135>  
 David J. Wilson  <https://orcid.org/0000-0001-9667-9449>  
 Allison Youngblood  <https://orcid.org/0000-0002-1176-3391>

## References

- Aarnio, A. N., Stassun, K. G., Hughes, W. J., & McGregor, S. L. 2011, *SoPh*, **268**, 195
- Airapetian, V. S., Glocer, A., Khazanov, G. V., et al. 2017, *ApJL*, **836**, L3
- Allard, F., Homeier, D., & Freytag, B. 2011, in ASP Conf. Ser. 448, 16th Cambridge Workshop on Cool Stars, Stellar Systems, and the Sun, ed. C. Johns-Krull, M. K. Browning, & A. A. West (San Francisco, CA: ASP), 91
- Anderson, D. R., Hellier, C., Gillon, M., et al. 2010, *ApJ*, **709**, 159
- Arnaud, K. A. 1996, in ASP Conf. Ser. 101, Astronomical Data Analysis Software and Systems V, ed. G. H. Jacoby & J. Barnes (San Francisco, CA: ASP), 17
- Arney, G. N., Meadows, V. S., Domagal-Goldman, S. D., et al. 2017, *ApJ*, **836**, 49
- Astropy Collaboration, Price-Whelan, A. M., Sipőcz, B. M., et al. 2018, *AJ*, **156**, 123
- Astropy Collaboration, Robitaille, T. P., Tollerud, E. J., et al. 2013, *A&A*, **558**, A33
- Astudillo-Defru, N., Delfosse, X., Bonfils, X., et al. 2017, *A&A*, **600**, A13
- Ballester, G. E., & Ben-Jaffel, L. 2015, *ApJ*, **804**, 116
- Barclay, T., Brande, J., Colon, K., et al. 2021, AAS Meeting Abstracts, **53**, 302.08
- Bayliss, D. D. R., Winn, J. N., Mardling, R. A., & Sackett, P. D. 2010, *ApJL*, **722**, L224
- Bean, J. L., Miller-Ricci Kempton, E., & Homeier, D. 2010, *Natur*, **468**, 669
- Berta, Z. K., Charbonneau, D., Désert, J.-M., et al. 2012, *ApJ*, **747**, 35
- Bonomo, A. S., Desidera, S., Benatti, S., et al. 2017, *A&A*, **602**, A107
- Brown, A., Froning, C. S., Youngblood, A., et al. 2022, *AJ*, **164**, 206
- Brown, D. J. A., Collier Cameron, A., Hall, C., Hebb, L., & Smalley, B. 2011, *MNRAS*, **415**, 605
- Bryson, S., Coughlin, J., Batalha, N. M., et al. 2020, *AJ*, **159**, 279
- Burkholder, J. B., Sander, S., Abbatt, J., et al. 2015, Technical Report 18, Jet Propulsion Laboratory, <https://hdl.handle.net/2014/45510>
- Burrows, A., & Orton, G. 2010, in Exoplanets, ed. S. Seager (Tucson, AZ: Univ. Arizona Press), 419
- Butler, R. P., Vogt, S. S., Laughlin, G., et al. 2017, *AJ*, **153**, 208
- Chapman, S. 1930, *Mem. Roy. Meteor.*, **3**, 103
- Chen, H., Zhan, Z., Youngblood, A., et al. 2021, *NatAs*, **5**, 298
- Cloutier, R., Astudillo-Defru, N., Bonfils, X., et al. 2019, *A&A*, **629**, A111
- Cortés-Zuleta, P., Rojo, P., Wang, S., et al. 2020, *A&A*, **636**, A98
- Crossfield, I. J. M., Waalkes, W., Newton, E. R., et al. 2019, *ApJL*, **883**, L16
- de Jager, C., Heise, J., Avgolopoulos, S., et al. 1986, *A&A*, **156**, 95
- Demangeon, O. D. S., Zapatero Osorio, M. R., Alibert, Y., et al. 2021, *A&A*, **653**, A41
- Des Marais, D. J., Harwit, M. O., Jucks, K. W., et al. 2002, *AsBio*, **2**, 153
- Domagal-Goldman, S. D., Segura, A., Claire, M. W., Robinson, T. D., & Meadows, V. S. 2014, *ApJ*, **792**, 90
- Dressing, C. D., & Charbonneau, D. 2015, *ApJ*, **807**, 45
- Duvvuri, G. M., Pineda, J. S., Berta-Thompson, Z. K., France, K., & Youngblood, A. 2023, *AJ*, **165**, 12
- Erkaev, N. V., Kulikov, Y. N., Lammer, H., et al. 2007, *A&A*, **472**, 329
- Fortney, J. J., Baraffe, I., & Militzer, B. 2010, in Exoplanets, ed. S. Seager, 397
- Fortney, J. J., Dawson, R. I., & Komacek, T. D. 2021, *JGRE*, **126**, e06629
- Fortney, J. J., Marley, M. S., & Barnes, J. W. 2007, *ApJ*, **659**, 1661
- Fortney, J. J., Saumon, D., Marley, M. S., Lodders, K., & Freedman, R. S. 2006, *ApJ*, **642**, 495
- Fossati, L., Erkaev, N. V., Lammer, H., et al. 2017, *A&A*, **598**, A90
- France, K., Arulanantham, N., Fossati, L., et al. 2018, *ApJS*, **239**, 16
- France, K., Bean, J. L., Berta-Thompson, Z. K., et al. 2020a, HST Proposal, Cycle 28, **16166**, HST
- France, K., Duvvuri, G., Egan, H., et al. 2020b, *AJ*, **160**, 237
- France, K., Fleming, B., Youngblood, A., et al. 2022, *JATIS*, **8**, 014006
- France, K., Froning, C. S., Linsky, J. L., et al. 2013, *ApJ*, **763**, 149
- France, K., Loyd, R. O. P., Youngblood, A., et al. 2016, *ApJ*, **820**, 89
- France, K., Stocke, J. T., Yang, H., et al. 2010, *ApJ*, **712**, 1277
- Fressin, F., Torres, G., Charbonneau, D., et al. 2013, *ApJ*, **766**, 81
- Froning, C. S., Kowalski, A., France, K., et al. 2019, *ApJL*, **871**, L26
- Fruscione, A., McDowell, J. C., Allen, G. E., et al. 2006, *Proc. SPIE*, **6270**, 62701V
- Fu, G., Sing, D. K., Lothringer, J. D., et al. 2022, *ApJL*, **925**, L3
- Fuhrmeister, B., Zisik, A., Schneider, P. C., et al. 2022, *A&A*, **663**, A119
- Gabriel, C., Denby, M., Fyfe, D. J., et al. 2004, in ASP Conf. Ser. 314, Astronomical Data Analysis Software and Systems (ADASS) XIII, ed. F. Ochsenbeim, M. G. Allen, & D. Egret (San Francisco, CA: ASP), 759
- Gaia Collaboration, Vallenari, A., Brown, A. G. A., et al. 2022, arXiv:2208.00211
- Gao, P., Hu, R., Robinson, T. D., Li, C., & Yung, Y. L. 2015, *ApJ*, **806**, 249
- Gao, P., Wakeford, H. R., Moran, S. E., & Parmentier, V. 2021, *JGRE*, **126**, e06655
- Gershberg, R. E. 1972, *Ap&SS*, **19**, 75
- Gillon, M., Triaud, A. H. M. J., Fortney, J. J., et al. 2012, *A&A*, **542**, A4
- Güdel, M., Audard, M., Reale, F., Skinner, S. L., & Linsky, J. L. 2004, *A&A*, **416**, 713
- Güdel, M., Audard, M., Skinner, S. L., & Horvath, M. I. 2002, *ApJL*, **580**, L73
- Hartman, J. D., Bakos, G. Á., Kipping, D. M., et al. 2011, *ApJ*, **728**, 138
- Hartman, J. D., Bakos, G. Á., Torres, G., et al. 2009, *ApJ*, **706**, 785
- Hawley, S. L., Fisher, G. H., Simon, T., et al. 1995, *ApJ*, **453**, 464
- He, C., Hörst, S. M., Lewis, N. K., et al. 2018, *ApJL*, **856**, L3
- He, L., Wang, S., Liu, J., et al. 2019, *ApJ*, **871**, 193
- Hellier, C., Anderson, D. R., Collier Cameron, A., et al. 2011, *A&A*, **535**, L7
- Howard, W. S., Teske, J., Corbett, H., et al. 2021, *AJ*, **162**, 147
- Hu, R., Seager, S., & Bains, W. 2012, *ApJ*, **761**, 166
- Hunter, J. D. 2007, *CSE*, **9**, 90
- Hunt-Walker, N. M., Hilton, E. J., Kowalski, A. F., Hawley, S. L., & Matthews, J. M. 2012, *PASP*, **124**, 545
- Husnoo, N., Pont, F., Mazeh, T., et al. 2012, *MNRAS*, **422**, 3151
- Jakosky, B. M., Grebrowsky, J. M., Luhmann, J. G., et al. 2015, *Sci*, **350**, 0210
- Jenkins, J. S., Díaz, M. R., Kurtovic, N. T., et al. 2020, *NatAs*, **4**, 1148
- Johnstone, C. P., Güdel, M., Stökl, A., et al. 2015, *ApJL*, **815**, L12
- Katsova, M. M., & Livshits, M. A. 2011, *ARep*, **55**, 1123
- Kawashima, Y., Hu, R., & Ikoma, M. 2019, *ApJL*, **876**, L5
- Kawashima, Y., & Ikoma, M. 2018, *ApJ*, **853**, 7
- Kiang, N. Y., Segura, A., Tinetti, G., et al. 2007, *AsBio*, **7**, 252
- Knutson, H. A., Howard, A. W., & Isaacson, H. 2010, *ApJ*, **720**, 1569
- Kopparapu, R. K. 2013, *ApJL*, **767**, L8
- Kopparapu, R. K., Ramirez, R., Kasting, J. F., et al. 2013, *ApJ*, **765**, 131
- Koskinen, T. T., Harris, M. J., Yelle, R. V., & Lavvas, P. 2013, *Icar*, **226**, 1678
- Kostov, V. B., Schlieder, J. E., Barclay, T., et al. 2019, *AJ*, **158**, 32
- Kowalski, A. F., Hawley, S. L., Holtzman, J. A., Wisniewski, J. P., & Hilton, E. J. 2010, *ApJL*, **714**, L98
- Kreidberg, L., Bean, J. L., Désert, J.-M., et al. 2014, *Natur*, **505**, 69
- Kunimoto, M., & Bryson, S. 2020, *RNAAS*, **4**, 83
- Lam, K. W. F., Faedi, F., Brown, D. J. A., et al. 2017, *A&A*, **599**, A3
- Lammer, H., Lichtenegger, H., Kulikov, Y., et al. 2007, *AsBio*, **7**, 185
- Line, M. R., Liang, M. C., & Yung, Y. L. 2010, *ApJ*, **717**, 496
- Linsky, J. 2019, *Host Stars and their Effects on Exoplanet Atmospheres*, Vol. 955 (Berlin: Springer)
- Linsky, J. L., Fontenla, J., & France, K. 2014, *ApJ*, **780**, 61
- Linsky, J. L., Wood, B. E., Youngblood, A., et al. 2020, *ApJ*, **902**, 3
- Linsky, J. L., Yang, H., France, K., et al. 2010, *ApJ*, **717**, 1291
- Lora, J. M., Kataria, T., & Gao, P. 2018, *ApJ*, **853**, 58
- Lothringer, J. D., & Barman, T. 2019, *ApJ*, **876**, 69
- Loyd, R. O. P., France, K., Youngblood, A., et al. 2016, *ApJ*, **824**, 102
- Loyd, R. O. P., France, K., Youngblood, A., et al. 2018, *ApJ*, **867**, 71
- Luque, R., Pallé, E., Kossakowski, D., et al. 2019, *A&A*, **628**, A39
- Madhusudhan, N., Agúndez, M., Moses, J. I., & Hu, Y. 2016, *SSRv*, **205**, 285
- Maxted, P. F. L., Anderson, D. R., Collier Cameron, A., et al. 2013, *PASP*, **125**, 48
- Mazeh, T., Holczer, T., & Faigler, S. 2016, *A&A*, **589**, A75
- Miguel, Y., & Kaltenegger, L. 2014, *ApJ*, **780**, 166
- Miguel, Y., Kaltenegger, L., Linsky, J. L., & Rugheimer, S. 2015, *MNRAS*, **446**, 345
- Miller-Ricci Kempton, E., Zahnle, K., & Fortney, J. J. 2012, *ApJ*, **745**, 3

- Modirrousta-Galian, D., Stelzer, B., Magaudda, E., et al. 2020, *A&A*, **641**, A113
- Moses, J. I., Visscher, C., Fortney, J. J., et al. 2011, *ApJ*, **737**, 15
- Munro, R. H., Gosling, J. T., Hildner, E., et al. 1979, *SoPh*, **61**, 201
- Murray-Clay, R. A., Chiang, E. I., & Murray, N. 2009, *ApJ*, **693**, 23
- Neupert, W. M. 1968, *ApJL*, **153**, L59
- Owen, J. E., & Jackson, A. P. 2012, *MNRAS*, **425**, 2931
- Owen, J. E., & Lai, D. 2018, *MNRAS*, **479**, 5012
- Owen, J. E., & Wu, Y. 2016, *ApJ*, **817**, 107
- Palle, E., Chen, G., Prieto-Arranz, J., et al. 2017, *A&A*, **602**, L15
- Peacock, S., Barman, T. S., Schneider, A. C., et al. 2022, *ApJ*, **933**, 235
- Pidhorodetska, D., Moran, S. E., Schwietzman, E. W., et al. 2021, *AJ*, **162**, 169
- Pont, F. 2009, *MNRAS*, **396**, 1789
- Poppenhaeger, K., & Wolk, S. J. 2014, *A&A*, **565**, L1
- Richey-Yowell, T., Shkolnik, E. L., Schneider, A. C., et al. 2019, *ApJ*, **872**, 17
- Rugheimer, S., Kaltenegger, L., Segura, A., Linsky, J., & Mohanty, S. 2015, *ApJ*, **809**, 57
- Salz, M. 2013, Chandra Proposal ID 15200435
- Salz, M. 2014, XMM-Newton Proposal ID 76346
- Salz, M., Schneider, P. C., Czesla, S., & Schmitt, J. H. M. M. 2015, *A&A*, **576**, A42
- Sanz-Forcada, J. 2016, XMM-Newton Proposal ID 80479
- Sanz-Forcada, J., Micela, G., Ribas, I., et al. 2011, *A&A*, **532**, A6
- Sato, B., Fischer, D. A., Henry, G. W., et al. 2005, *ApJ*, **633**, 465
- Schmitt, J. H. M. M., Haisch, B., & Barwig, H. 1993, *ApJL*, **419**, L81
- Schneider, A. C., & Shkolnik, E. L. 2018, *AJ*, **155**, 122
- Schweitzer, A., Passegger, V. M., Cifuentes, C., et al. 2019, *A&A*, **625**, A68
- Schwietzman, E. W., Kiang, N. Y., Parenteau, M. N., et al. 2018, *AsBio*, **18**, 663
- Segura, A., Kasting, J. F., Meadows, V., et al. 2005, *AsBio*, **5**, 706
- Segura, A., Walkowicz, L. M., Meadows, V., Kasting, J., & Hawley, S. 2010, *AsBio*, **10**, 751
- Shkolnik, E. L., Barman, T. S., Meadows, V. S., Pagano, I., & Peacock, S. 2016, HST Proposal, Cycle 24, 14784, HST
- Skaf, N., Bieger, M. F., Edwards, B., et al. 2020, *AJ*, **160**, 109
- Smith, R. K., Brickhouse, N. S., Liedahl, D. A., & Raymond, J. C. 2001, *ApJL*, **556**, L91
- Smithsonian Astrophysical Observatory 2000, SAOImage DS9: A utility for displaying astronomical images in the X11 window environment, Astrophysics Source Code Library, ascl:0003.002
- Sohn, S. T., Bostroem, K. A., Proffitt, C., et al. 2019, Technical Report7, Space Telescope Science Institute
- Spake, J. J., Sing, D. K., Wakeford, H. R., et al. 2021, *MNRAS*, **500**, 4042
- Stelzer, B. 2020, Complete high-energy census of the cool stellar neighbors, XMM-Newton Proposal ID, #88102
- Szabó, G. M., & Kiss, L. L. 2011, *ApJL*, **727**, L44
- Teal, D. J., Kempton, E. M. R., Bastelberger, S., Youngblood, A., & Arney, G. 2022, *ApJ*, **927**, 90
- JWST Transiting Exoplanet Community Early Release Science Team, Ahrer, E.-M., Alderson, L., et al. 2023, *Natur*, **614**, 649
- Tian, F., France, K., Linsky, J. L., Mauas, P. J. D., & Vieytes, M. C. 2014, *E&PSL*, **385**, 22
- Tilley, M. A., Segura, A., Meadows, V., Hawley, S., & Davenport, J. 2019, *AsBio*, **19**, 64
- Traub, W. A. 2012, *ApJ*, **745**, 20
- Tsai, S.-M., Lee, E. K. H., Powell, D., et al. 2022, *Natur*, **617**, 483
- Venot, O., Fray, N., Bénilan, Y., et al. 2013, *A&A*, **551**, A131
- Vidal-Madjar, A., Désert, J. M., Lecavelier des Etangs, A., et al. 2004, *ApJL*, **604**, L69
- Virtanen, P., Gommers, R., Oliphant, T. E., et al. 2020, *NatMe*, **17**, 261
- Wood, B. E., Redfield, S., Linsky, J. L., Müller, H.-R., & Zank, G. P. 2005, *ApJS*, **159**, 118
- Woods, T. N., Chamberlin, P. C., Harder, J. W., et al. 2009, *GeoRL*, **36**, L01101
- Woods, T. N., Eparvier, F. G., Hock, R., et al. 2012, *SoPh*, **275**, 115
- Wright, N. J., Drake, J. J., Mamajek, E. E., & Henry, G. W. 2011, *ApJ*, **743**, 48
- Wright, N. J., Newton, E. R., Williams, P. K. G., Drake, J. J., & Yadav, R. K. 2018, *MNRAS*, **479**, 2351
- Yelle, R., Lammer, H., & Ip, W.-H. 2008, *SSRv*, **139**, 437
- Youngblood, A., France, K., Loyd, R. O. P., et al. 2016, *ApJ*, **824**, 101
- Youngblood, A., Pineda, J. S., Ayres, T., et al. 2022, *ApJ*, **926**, 129
- Zahnle, K., Marley, M. S., Freedman, R. S., Lodders, K., & Fortney, J. J. 2009, *ApJL*, **701**, L20